

Numerical study of anisotropic diffusion in Turing patterns based on Finsler geometry modeling

Gildas Diguët

*Micro System Integration Center, Tohoku University, Sendai, Japan*Madoka Nakayama *Research Center of Mathematics for Social Creativity, Research Institute for Electronic Science, Hokkaido University, Sapporo, Japan*Sohei Tasaki *Department of Mathematics, Faculty of Science, Hokkaido University, Sapporo, Japan*Fumitake Kato and Hiroshi Koibuchi **National Institute of Technology (KOSEN), Ibaraki College, Hitachinaka, Japan*

Tetsuya Uchimoto

*Institute of Fluid Science (IFS), Tohoku University, Sendai, Japan
and ELYTMAX, CNRS-Universite de Lyon-Tohoku University, Sendai, Japan* (Received 30 May 2023; revised 26 October 2023; accepted 11 December 2023; published 10 January 2024)

We numerically study the anisotropic Turing patterns (TPs) of an activator-inhibitor system described by the reaction-diffusion (RD) equation of Turing, focusing on anisotropic diffusion using the Finsler geometry (FG) modeling technique. In FG modeling, the diffusion coefficients are dynamically generated to be direction dependent owing to an internal degree of freedom (IDOF) and its interaction with the activator and inhibitor. Because of this dynamical diffusion coefficient, FG modeling of the RD equation sharply contrasts with the standard numerical technique in which direction-dependent coefficients are manually assumed. To find the solution of the RD equations in FG modeling, we use a hybrid numerical technique combining the Metropolis Monte Carlo method for IDOF updates and discrete RD equations for steady-state configurations of the activator-inhibitor variables. We find that the newly introduced IDOF and its interaction are a possible origin of spontaneously emergent anisotropic patterns of living organisms, such as zebra and fishes. Moreover, the IDOF makes TPs controllable by external conditions if the IDOF is identified with the direction of cell diffusion accompanied by thermal fluctuations.

DOI: [10.1103/PhysRevE.109.014213](https://doi.org/10.1103/PhysRevE.109.014213)**I. INTRODUCTION**

Turing patterns (TPs) are described by the partial differential equations of Turing [1] for two different variables u and v , which are scalar functions on a domain in \mathbf{R}^2 . These u and v variables are usually called the activator and inhibitor, respectively [2–5], owing to their interaction properties, as implemented in the reaction and diffusion (RD) terms in the equations. TPs emerge in the macroscopic [6–8] to microscopic [9,10] scale range.

These patterns emerge because of competition between activators and inhibitors, as well as their diffusion and reaction, and many studies have been conducted to extend the Laplace operators of the RD equation to the graph Laplacian to find TPs in random networks [11–15]. Another extension is to modify the diffusivity to accommodate the non-Gaussian behavior of Brownian particles confined between narrow plates by including fluctuations in the diffusion constants such that

position-dependent and anisotropic diffusion emerges [16]. Such a non-Gaussian distribution of particle displacements is considered anomalous diffusion, corresponding to anomalous transport phenomena in crowded biological materials, such as cellular membranes [17–20]. This anomalous transport is characterized by subdiffusion, which is described by the power-law behavior of the mean-square displacement $\sim t^\alpha$ ($0 < \alpha < 1$) observed at intermediate timescales. Superdiffusion characterized by t^α ($\alpha > 1$) is observed in bacterial swarming [21,22]. This phenomenon is described by the Levy walk, which is a model of a random walk with a constant speed.

Anisotropic TPs, which are steady-state solutions of RD equation with a periodicity in a spatial direction, are observed on zebra and fish (Fig. 1). The anisotropic TPs are known to emerge because of the differences in the diffusion constants between the activator and inhibitor with direction-dependent diffusion. The difference in the diffusion constants corresponding to marine angelfish was estimated by Kondo and Asai in Ref. [23]. In Refs. [24,25], Shoji *et al.* reported that anisotropy in the diffusion constants is the origin of

*Corresponding author: koi-hiro@sendai-nct.ac.jp

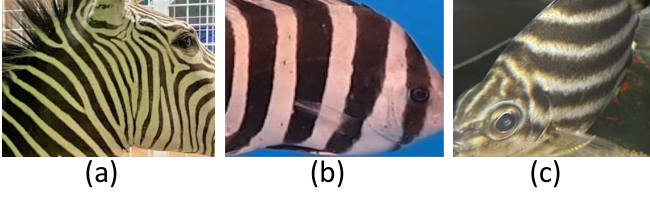


FIG. 1. Anisotropic TPs on (a) zebra and [(b) and (c)] fishes. The patterns vary depending on the individual, while the direction of the patterns depends only on the species.

anisotropic TPs and is effective in determining the direction of stripe patterns in numerical studies. TPs appear on curved surfaces [26]. Krause *et al.* reported that the anisotropy in the evolution of TPs is sensitive to the curvature of the growing domains, which are two-dimensional curved surfaces embedded in \mathbf{R}^3 , assuming that the induced metric describes the Laplace-Beltrami operator in the diffusion terms [27,28].

Pattern anisotropy is numerically producible by assuming direction-dependent diffusion constants, as described above, because the underlying reason for these stripe TPs is well understood to be anisotropic diffusion. However, the origin of anisotropic diffusion remains unclear. Therefore, the phenomenological description of anisotropic diffusion is not always satisfactory.

In this paper, we study the origin of anisotropic diffusion in TPs. For this purpose, we focus on the mechanism of dynamic anisotropy, in which the diffusion constants dynamically appear as direction-dependent constants [29,30]. Here we recall that such a dynamic anisotropy has been successfully implemented in the interaction coefficients in several statistical mechanical models using the Finsler geometry (FG) modeling technique [31–35]. In these statistical mechanical models, the dynamically implemented interaction coefficients can be controlled under external conditions. Therefore, we expect that the anisotropic diffusion of the RD equation is also controlled by external conditions, such as mechanical forces, if FG modeling is applied to the diffusion terms of the RD equation. Thus, the FG modeling technique allows us to study the control of the TP direction by external conditions, and we consider that this new modeling technique has an advantage over phenomenological modeling in which diffusion anisotropy is manually implemented.

This paper is organized as follows: In Sec. II, we review the FitzHugh-Nagumo-type RD equation for the variables u and v from a numerical point of view and show numerical data, such as snapshots of isotropic and anisotropic TPs, obtained on a regular square lattice of size $N = 100^2$, where anisotropic TPs appear owing to the assumed direction-dependent diffusion coefficients in the RD equations. To quantify the anisotropic TPs and evaluate the effect of the direction-dependent diffusion coefficients, we introduce absolute second-order derivatives of u and v as well as the squares of the first-order derivatives. In Sec. III, we introduce the FG modeling technique to dynamically implement diffusion anisotropy in the Laplace operator in the RD equation by including a new internal degree of freedom (IDOF) on two types of lattices: fixed-connectivity and dynamically triangulated lattices. A numerical technique, which we call the

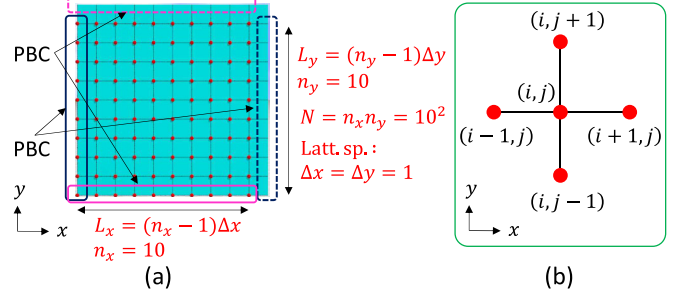


FIG. 2. (a) Regular square lattice with PBCs of size $N = 10^2$, which is small compared with the value of $N = 100^2$ assumed in the simulations in the following subsection, and (b) lattice site (i, j) and its four nearest-neighbor sites, where $1 \leq i \leq n_x$ and $1 \leq j \leq n_y$. The lattice spacing is assumed to be $\Delta x = \Delta y = 1$ in the simulations.

hybrid technique, is introduced to update u , v and the new IDOF. In Sec. IV, we present the numerical data, including snapshots obtained on these two lattices. Finally, we discuss possible techniques for controlling the pattern direction that emerge because of the dynamical anisotropy. The results and conclusion are summarized in Sec. V.

II. STANDARD APPROACH TO TURING PATTERNS

In this section, we review TPs described by the FitzHugh-Nagumo equation on regular square lattices with periodic boundary conditions (PBCs) [Figs. 2(a) and 2(b)].

A. FitzHugh-Nagumo equation with diffusion anisotropy

Let $u(x, y)$ and $v(x, y)$ be the variables corresponding to the activator and inhibitor, respectively, which satisfy the FitzHugh-Nagumo-type RD equation

$$\begin{aligned} \frac{\partial u}{\partial t} &= D_u \Delta u + f(u, v), & f &= u - u^3 - v, \\ \frac{\partial v}{\partial t} &= D_v \Delta v + \gamma g(u, v), & g &= u - \alpha v, \end{aligned} \quad (1)$$

on the two-dimensional plane [24,25]. The first and second terms on the right-hand side are called the diffusion and reaction terms, respectively, where $\Delta = \frac{\partial^2}{\partial x^2} + \frac{\partial^2}{\partial y^2}$ is the Laplace operator. The symbols D_u and D_v are the diffusion coefficients, and α and γ are constants.

For a suitable range of parameters, the RD equations have certain steady-state solutions called TPs with periodicity in spatial directions. When the periodicity appears almost regularly in one direction, the patterns become anisotropic, as shown in Figs. 1(a)–1(c). These anisotropic patterns can be reproduced by using the RD equation with diffusion anisotropy introduced through the parameters a and b [25]:

$$\begin{aligned} \Delta u &\rightarrow \Delta_a u = a \frac{\partial^2 u}{\partial x^2} + (2-a) \frac{\partial^2 u}{\partial y^2}, & (0 < a < 2), \\ \Delta v &\rightarrow \Delta_b v = b \frac{\partial^2 v}{\partial x^2} + (2-b) \frac{\partial^2 v}{\partial y^2}, & (0 < b < 2). \end{aligned} \quad (2)$$

For the ranges $0 < a < 2$ and $0 < b < 2$, the diffusion constants D_u and D_v in Eq. (1) effectively become direction

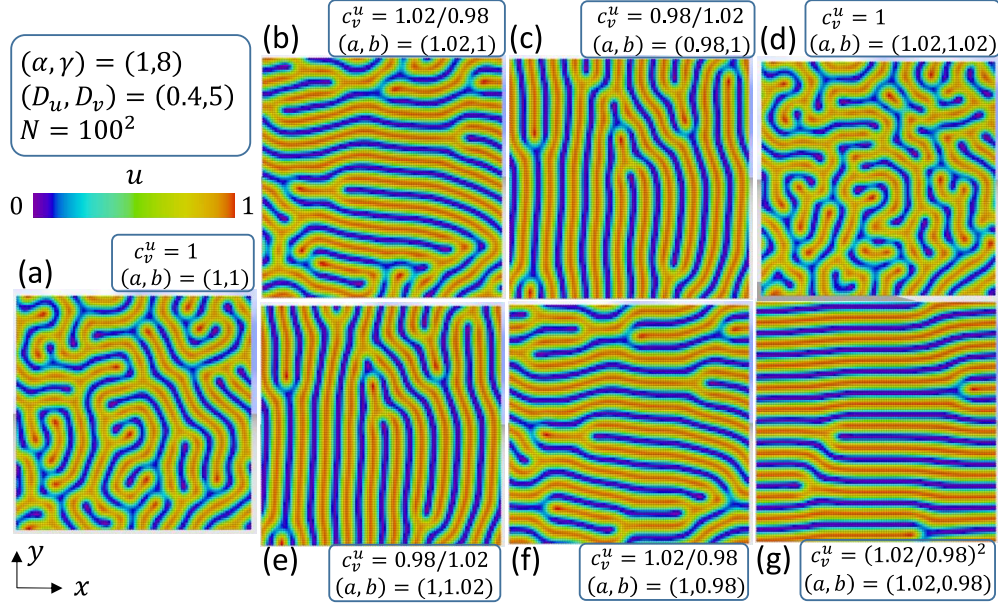


FIG. 3. Snapshots of the standard model on a regular square lattice of size $N = 100^2$ with PBCs. The parameters (a, b) and c_v^u in Eq. (4) are shown in (a)–(g). The pattern is isotropic when $a = b$, as in (a) and (d), represented by $c_v^u = 1$, while the stripe lies along the x direction when $a > b$, as in (b), (f), and (g), represented by $c_v^u > 1$, and it lies along the y direction when $a < b$, as in (c) and (e), represented by $c_v^u < 1$.

dependent:

$$\begin{aligned} D_u &\rightarrow (D_u^x, D_u^y) = (aD_u, (2-a)D_u), \\ D_v &\rightarrow (D_v^x, D_v^y) = (bD_v, (2-b)D_v). \end{aligned} \quad (3)$$

The direction dependence of D_u and D_v is characterized by the anisotropy

$$\begin{aligned} c_v^u &= \frac{c_u}{c_v} = \frac{a(2-b)}{b(2-a)}, \quad \text{where} \quad c_u = \frac{D_u^x}{D_u^y} = \frac{a}{2-a}, \\ c_v &= \frac{D_v^x}{D_v^y} = \frac{b}{2-b}. \end{aligned} \quad (4)$$

Note that the conditions $a = b = 1$ describing isotropic diffusion are represented by $c_v^u = 1$. The isotropic condition $c_v^u = 1$ is expected for all $a = b$ even when $a \neq 1$, where $c_u \neq 1$ and $c_v \neq 1$.

B. Numerical solutions on a regular square lattice with periodic boundary conditions

The discrete time-evolution equations corresponding to Eq. (1) are given by

$$\begin{aligned} u_{ij}(t + \Delta t) &\leftarrow u_{ij}(t) + \Delta t [D_u \Delta_a u_{ij}(t) + f(u_{ij}(t), v_{ij}(t))], \\ v_{ij}(t + \Delta t) &\leftarrow v_{ij}(t) + \Delta t [D_v \Delta_b v_{ij}(t) + g(u_{ij}(t), v_{ij}(t))], \end{aligned} \quad (5)$$

where u_{ij} and v_{ij} denote the discrete analogs of $u(x, y)$ and $v(x, y)$ at lattice site (i, j) ($1 \leq i \leq n_x, 1 \leq j \leq n_y$) [Fig. 2(a)]. The discrete diffusion terms $\Delta_a u_{ij}$ and $\Delta_b v_{ij}$ are given by

$$\begin{aligned} \Delta_a u_{ij} &= \frac{a}{(\Delta x)^2} (u_{i+1,j} + u_{i-1,j} - 2u_{i,j}) \\ &\quad + \frac{2-a}{(\Delta y)^2} (u_{i,j+1} + u_{i,j-1} - 2u_{i,j}), \end{aligned}$$

$$\begin{aligned} \Delta_b v_{ij} &= \frac{b}{(\Delta x)^2} (v_{i+1,j} + v_{i-1,j} - 2v_{i,j}) \\ &\quad + \frac{2-b}{(\Delta y)^2} (v_{i,j+1} + v_{i,j-1} - 2v_{i,j}), \end{aligned} \quad (6)$$

with lattice spacings Δx and Δy . The convergent criteria of the iterations in Eq. (5) are given by

$$\begin{aligned} \text{Max}\{|u_{ij}(t + \Delta t) - u_{ij}(t)|\} &< 1 \times 10^{-8}, \\ \text{Max}\{|v_{ij}(t + \Delta t) - v_{ij}(t)|\} &< 1 \times 10^{-8}. \end{aligned} \quad (7)$$

Snapshots of the convergent configurations of u on the lattice of size $N = 100^2$ ($\Leftrightarrow n_x = n_y = 100$) are plotted in Figs. 3(a)–3(g), where

$$\Delta t = 1 \times 10^{-3}, \quad \Delta x = \Delta y = 1. \quad (8)$$

The value of u in the snapshots is normalized to $[0, 1]$. We confirm that the patterns are isotropic when $a = b$ in Fig. 3(a) $a = b = 1$ and Fig. 3(d) $a = b = 1.02$, while they are anisotropic when $a > b$ in Figs. 3(b) and 3(f) and $a < b$ in Figs. 3(c) and 3(e). This change from isotropy to anisotropy is enhanced when the anisotropy c_v^u is increased from $c_v^u = 1$ in Fig. 3(a) to $c_v^u = 1.02/0.98$ in Fig. 3(b) and $c_v^u = (1.02/0.98)^2$ in Fig. 3(g). We find from Figs. 3(b) and 3(f) [from Figs. 3(c) and 3(e)] that the increase (\nearrow) in a and the decrease (\searrow) in b (the decrease (\searrow) in a and the increase (\nearrow) in b) cause the same effect, enforcing the pattern anisotropy along the x direction (the y direction). These effects are consistent with the observation that the anisotropy of the pattern in Fig. 3(g) is stronger than that in Figs. 3(b) and 3(f). These opposite or competing behaviors of u and v are obtained because of the direction-dependent diffusion constants in Eq. (3). Therefore, the direction dependence of diffusion coefficients and the resulting behaviors of u and v will be used to introduce dynamical anisotropy in FG modeling in the following section.

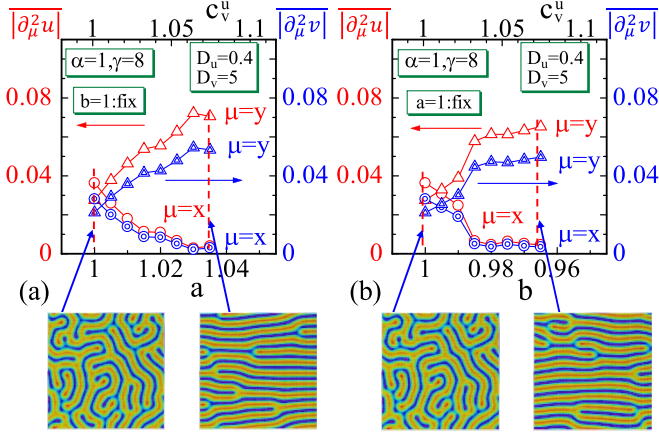


FIG. 4. $|\overline{\partial_\mu^2 u}|$ and $|\overline{\partial_\mu^2 v}|$ obtained with (a) a variation under the conditions $a \geq b(=1)$ and (b) b variation under $(1=a) \geq b$ on the $N = 100^2$ lattice, where 1×10^{-7} is assumed in Eq. (7). The upper axes represent the scale of anisotropy c_v^u .

To quantify the observed anisotropy in the TPs, we calculate the mean absolute values of the second-order partial differentials of u and v ,

$$\begin{aligned} |\overline{\partial_x^2 u}| &= \frac{1}{N} \sum_{ij} |u_{i+1,j} + u_{i-1,j} - 2u_{i,j}|, \\ |\overline{\partial_y^2 u}| &= \frac{1}{N} \sum_{ij} |u_{i,j+1} + u_{i,j-1} - 2u_{i,j}|, \\ |\overline{\partial_x^2 v}| &= \frac{1}{N} \sum_{ij} |v_{i+1,j} + v_{i-1,j} - 2v_{i,j}|, \\ |\overline{\partial_y^2 v}| &= \frac{1}{N} \sum_{ij} |v_{i,j+1} + v_{i,j-1} - 2v_{i,j}|. \end{aligned} \quad (9)$$

Figure 4(a) shows $|\overline{\partial_\mu^2 u}|$ and $|\overline{\partial_\mu^2 v}|$ ($\mu = x, y$) calculated by varying a under the conditions $b = 1$ and $a \geq 1$. We find that $|\overline{\partial_x^2 u}|$ and $|\overline{\partial_x^2 v}|$ decrease (\searrow) and that $|\overline{\partial_y^2 u}|$ and $|\overline{\partial_y^2 v}|$ increase (\nearrow) with increasing a (\nearrow). The results plotted in Fig. 4(b) also show how $|\overline{\partial_\mu^2 u}|$ and $|\overline{\partial_\mu^2 v}|$ vary when b decreases (\searrow) under the conditions $a = 1$ and $b \leq 1$.

This behavior $|\overline{\partial_x^2 u}| < |\overline{\partial_y^2 u}|$ is also understood from the fact that the direction-dependent diffusion constants $(D_u^x, D_u^y) = (aD_u, (2-a)D_u)$ in Eq. (3) obey $D_u^x > D_u^y$ for $a > 1$ and $b = 1$ because a large diffusion constant D_u^x induces a long-distance spatial correlation of u , implying almost constant u along the x axis, which is reflected in a small $|\overline{\partial_x^2 u}|$. Thus, the observed data $|\overline{\partial_\mu^2 u}|$ indicate that the u anisotropy is consistent with the physical stability condition for energy minimization. This consistency in the u anisotropy is understood from the fact that the RD equation for u in Eq. (1) is connected with the Ginzburg-Landau Cahn-Hilliard energy functional [36].

In contrast, the data $|\overline{\partial_\mu^2 v}|$ plotted in Fig. 4(b) have an opposite response to the diffusion coefficients; v anisotropy is observed in the x direction, causing $|\overline{\partial_x^2 v}| > |\overline{\partial_y^2 v}|$ under the condition $D_v^x < D_v^y$ for $b < 1(=a)$ for $(D_v^x, D_v^y) = (bD_v, (2-b)D_v)$ in Eq. (3). The anisotropies in the diffusion constants in

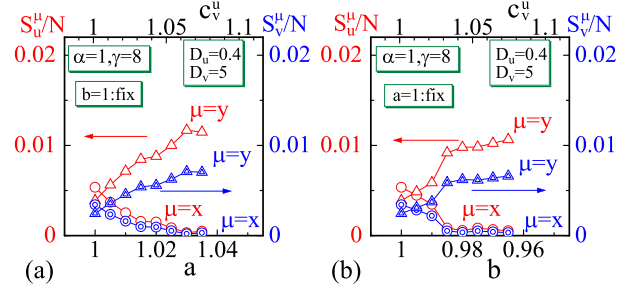


FIG. 5. S_u^μ , ($\mu = x, y$) and S_v^μ , ($\mu = x, y$) obtained with (a) a variation under the conditions $a \geq b(=1)$ and (b) b variation under $(1=a) \geq b$ on the $N = 100^2$ lattice. The upper axes represent the scale of anisotropy c_v^u . The assumed parameters are the same as those in Fig. 4.

Eq. (3) can also be reflected in the quantities

$$\begin{aligned} S_u^x &= \frac{1}{4} \sum_{ij} (u_{i+1,j} - u_{i-1,j})^2, & S_u^y &= \frac{1}{4} \sum_{ij} (u_{i,j+1} - u_{i,j-1})^2, \\ S_v^x &= \frac{1}{4} \sum_{ij} (v_{i+1,j} - v_{i-1,j})^2, & S_v^y &= \frac{1}{4} \sum_{ij} (v_{i,j+1} - v_{i,j-1})^2. \end{aligned} \quad (10)$$

The plots in Figs. 5(a) and 5(b) are consistent with those in Figs. 4(a) and 4(b). Moreover, we find that the result $S_{u,v}^x < S_{u,v}^y$ is caused under $D_u^x > D_u^y$ in Fig. 5(a), while $S_{u,v}^x < S_{u,v}^y$ is caused under $D_v^x < D_v^y$ in Fig. 5(b). These opposite behaviors in $S_{u,v}^{x,y}$ and $S_{v,u}^{x,y}$ in response to D_u^x and D_v^x come from the competing property of u and v , as emphasized above.

III. FINSLER GEOMETRY MODELING OF TURING PATTERNS

A. Finsler geometry modeling of anisotropic diffusion

FG modeling modifies length scales so that interactions of the variables u and v are direction dependent by using the IDOF $\vec{\tau} (\in S^2/2$: half sphere). The new IDOF $\vec{\tau}$ (nonpolar variable) comes from movements of vertices of triangulated “fixed” and “fluid” lattices (Figs. 18 and 19), and $\vec{\tau}$ is used to define the discrete Laplace operators

$$\begin{aligned} \Delta u_i &= 2 \left(\sum_{j(i)} \gamma_{ij}^u u_j - u_i \sum_{j(i)} \gamma_{ij}^u \right), \\ \Delta v_i &= 2 \left(\sum_{j(i)} \gamma_{ij}^v v_j - u_i \sum_{j(i)} \gamma_{ij}^v \right), \quad (1 \leq i \leq N). \end{aligned} \quad (11)$$

The sum $\sum_{j(i)}$ is over vertices j connected to i , and the $\gamma_{ij}^{u,v}$ values depend on the unit Finsler length determined by $\vec{\tau}$ (Appendix B). We use these Laplace operators to define modified RD equations, which will be introduced in the following subsection, corresponding to those in Eq. (1) (Appendix C).

To update $\bar{\tau}$ with the Monte Carlo (MC) procedure, we assume the following discrete Hamiltonian (Appendix D):

$$S(\bar{r}; \bar{\tau}) = \begin{cases} \gamma S_1 + U_V + D_u S_u + D_v S_v + \lambda S_\tau + S_\tau^F, & (\gamma = 1), \quad (\text{fixed}) \\ \gamma S_1 + U_V + U_{\mathcal{T}} + D_u S_u + D_v S_v + \lambda S_\tau + S_\tau^F, & (\gamma = 1), \quad (\text{fluid}), \end{cases} \quad (12)$$

where $S(\bar{r}; \bar{\tau})$ denotes that the variables \bar{r} and $\bar{\tau}$ are not independent (Appendix A). The tension coefficient γ of S_1 is assumed to be $\gamma = 1$ for simplicity. The difference in S between the fixed and fluid models in Eq. (12) is that a potential $U_{\mathcal{T}}$ is included in S for the fluid model, where the symbol \mathcal{T} denotes a triangulation (Appendix A). The partition functions are written as

$$\begin{aligned} Z_{\text{fix}} &= \int \prod_i d\bar{r}_i \exp(-S), \quad (\text{fixed model}), \\ Z_{\text{flu}} &= \sum_{\mathcal{T}} \int \prod_i d\bar{r}_i \exp(-S), \quad (\text{fluid model}), \end{aligned} \quad (13)$$

where $\int \prod_{i=1}^N d\bar{r}_i$ denotes $2N$ -dimensional multiple integrations on a domain in \mathbf{R}^2 and $\sum_{\mathcal{T}}$ in Z_{flu} denotes the sum over all possible triangulations.

The simulation unit is given by $k_B T = 1$, where k_B is the Boltzmann constant and T is the temperature. The Gaussian bond potential S_1 is defined by the squared bond length $\gamma \ell^2$ with tension coefficient $\gamma = 1$ (Appendices D and E), and hence, this ℓ can also be expressed by the lattice spacing denoted by d (Fig. 17 in Appendix A), which corresponds to $\Delta x (=1)$ and $\Delta y (=1)$ in Eq. (8). From the dependence of S_1 on d , the surface tension σ also depends on d (Appendix E). Note also that these simulation units, $k_B T (= 1)$ for energy and d for length, are used only in the MC simulations for τ updates.

B. Hybrid numerical technique

We introduce a numerical technique to find steady state configurations of u and v under the presence of IDOF $\bar{\tau}$ on two types of triangulated lattices: fixed and fluid (Appendix A). The variables u_i and v_i are updated as follows:

$$\begin{aligned} u_i(t + \Delta t) &\leftarrow u_i(t) + \Delta t [D_u \Delta u_i(t) + f(u_i(t), v_i(t))], \\ v_i(t + \Delta t) &\leftarrow v_i(t) + \Delta t [D_v \Delta v_i(t) + g(u_i(t), v_i(t))], \end{aligned} \quad (14)$$

where the diffusion terms are given by Eq. (11). Direction dependence is not manually introduced into these diffusion terms, in sharp contrast to those in Eq. (6). Here we should note that the RD equation in Eq. (14) has no dependence on the lattice spacing d , because d (Fig. 17) is not included in the Laplacian in Eq. (11). In other words, the Laplacian in Eq. (11) is defined to be influenced only by the lattice size N , as in the case of the model on the regular square lattice with $\Delta x = 1$ and $\Delta y = 1$.

The hybrid numerical technique is summarized in the following five steps:

(i) The discrete time evolution of Eq. (14) is iterated with the diffusion terms Δu_i and Δv_i in Eq. (11) with coefficients D_u and D_v .

(ii) In each discrete time step $t \rightarrow t + \Delta t$, the variables $\{\bar{r}_i\}$ are updated once in MC simulations using S in Eq. (12), as shown in Fig. 4(c), on a fixed connectivity lattice (fixed

model) or on a dynamically triangulated fluid lattice (fluid model), which are defined by the partition functions in Eq. (13). At each update of \bar{r}_i , the variable $\bar{\tau}_i$ is also updated by using $\Delta \bar{r}_i (= \bar{r}_i(\text{new}) - \bar{r}_i(\text{old}))$ [Fig. 18(d)].

(iii) Steps (i) and (ii) are repeated n_{MC} times, where n_{MC} is suitably large.

(iv) Step (i) is repeated under the final configurations of $\{\bar{\tau}_i\}$ in (iii) until the convergent criteria are satisfied:

$$\begin{aligned} \text{Max}\{|u_i(t + \Delta t) - u_i(t)|\} &< 1 \times 10^{-8}, \\ \text{Max}\{|v_i(t + \Delta t) - v_i(t)|\} &< 1 \times 10^{-8}, \quad (1 \leq i \leq N), \\ \Delta t &= 0.001, \end{aligned} \quad (15)$$

which are the same as those in Eqs. (7) and (8) for the standard model.

(v) Steps (i)–(iv) are repeated n_{itr} times to calculate the mean values of physical quantities using the convergent configurations obtained in step (iv). The initial configurations of the variables u , v and $\bar{\tau}$ are randomly fixed using uniform random numbers such that $u, v \in \{-0.5, 0.5\}$ and $\bar{\tau} \in S^1$: unit circle.

Notably, the configurations of u , v and $\bar{\tau}$ obtained in steps (i) and (ii) are used as the initial configurations of step (iv) for the RD equations of u and v . This implies that a canonical ensemble configuration of IDOF $\bar{\tau}$ under fluctuating u, v is assumed for the initial configuration of the RD equation in step (iv). The u and v during the MC update of $\bar{\tau}$ are not convergent in terms of the criteria in Eq. (15); however, the patterns are close to those in the convergent steady state.

IV. RESULTS

As described in the final part of the preceding Sec. III A, the Gaussian bond potential S_1 depends on the lattice spacing d (Fig. 17) in the MC process for $\bar{\tau}$. For this reason, to check whether the results are influenced by σ , we use two different values of d :

$$\begin{aligned} d &= 0.525 \quad (\Leftrightarrow \langle \ell^2 \rangle \simeq \frac{1}{2} \Leftrightarrow \sigma > 0), \\ d &= 0.41 \quad (\Leftrightarrow \langle \ell^2 \rangle \simeq \frac{1}{3} \Leftrightarrow \sigma \simeq 0). \end{aligned} \quad (16)$$

The mean-squared bond lengths $\langle \ell^2 \rangle$ inside the parenthesis are numerically obtained under the assumed d . The expression of σ is given by $\sigma = (3N/A)(\langle \ell^2 \rangle - \frac{1}{3})$ in Eq. (E5) (Appendix E), where the surface area $A = L_x L_y = (n_x - 1)(n_y - 1)d^2$ depends on n_x , n_y , and d [Fig. 2(a)]. In the hybrid simulations, to see the effect of d on σ , we vary d as in Eq. (16) with fixed n_x and n_y .

A. Snapshots

Steps (i) to (iv) described in Sec. III B are iterated once to obtain snapshots in this subsection. Figures 6(a)–6(d) show snapshots of the variable u without (upper row) and with $\bar{\tau}$

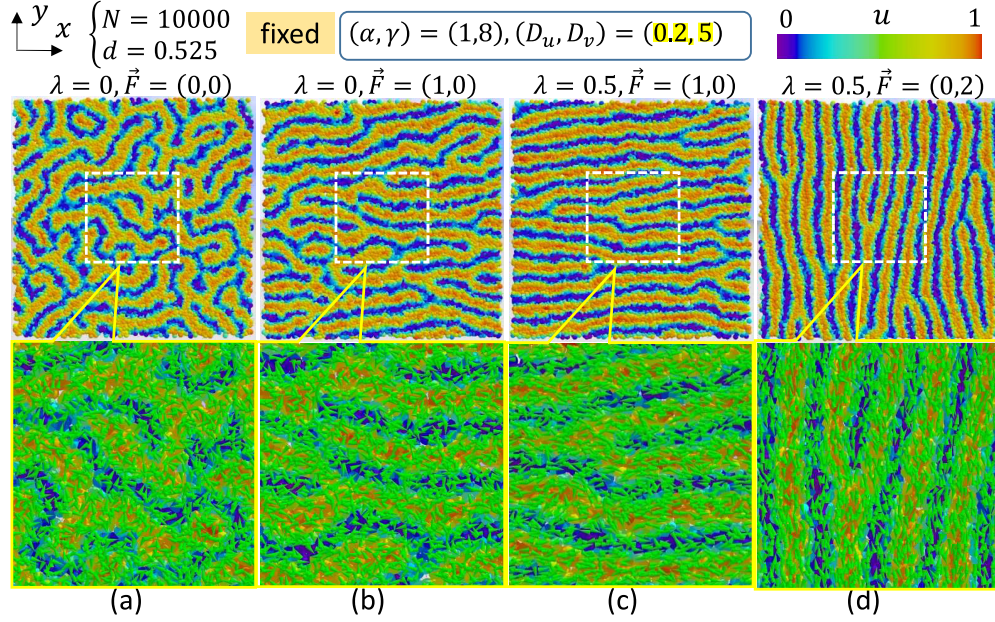


FIG. 6. Snapshots of TPs for u obtained on a fixed lattice of size $N = 10\,000$ with lattice spacing $d = 0.525$. The assumed parameters are shown in the figure. The upper rows show the normalized $u \in [0, 1]$ indicated by the color code without the IDOF $\vec{\tau}$, and the lower row shows enlarged views with $\vec{\tau}$ of the central region enclosed by the dashed rectangles, in which $\vec{\tau}$ variables are represented by small cones.

(lower row) the IDOF of the fixed model on the $N = 10\,000$ lattice for the lattice spacing $d = 0.525$. The values of u are normalized in the range $[0, 1]$, as shown in the color code. These snapshots are obtained by varying λ and \vec{F} . The other parameters are fixed to $(\alpha, \gamma) = (1, 8)$ and $(D_u, D_v) = (0.4, 5)$. The χ_0 in Eq. (B2) is assumed to be $\chi_0 = 0.5$.

When $\lambda = 0$ and $\vec{F} = (0, 0)$, the fluctuation direction of $\vec{\tau}$ is expected to be random, causing a random IDOF $\vec{\tau}$. In this case, an isotropic pattern is confirmed in Fig. 6(a), where the $\vec{\tau}$ variables in the snapshots of the central region are plotted with small cones. When \vec{F} is increased to $\vec{F} = (1, 0)$ [Fig. 6(b)], $\vec{\tau}$ is slightly aligned along the x direction, which becomes clear for $\lambda = 0.5$ [Fig. 6(c)]. The pattern is also forced to be more anisotropic by enlarging $\vec{F} = (0, 0)$ to $\vec{F} = (0, 2)$, where the direction is changed to along the y axis. From these snapshots, we find that the isotropy and anisotropy in the patterns is determined by the fluctuation direction $\vec{\tau}$ of the vertices. This finding indicates that the FG modeling effectively modifies the diffusion constants D_u and D_v to be anisotropic. These effective diffusion constants are numerically extracted in the following subsection. Notably, the patterns of v are almost the same as those of u plotted in Fig. 6. The patterns obtained with $d = 0.41$ corresponding to $\sigma \simeq 0$ in Eq. (16) are almost the same as those in Fig. 6, and we therefore find that the patterns are not influenced by isotropic σ , as expected. The influence of σ on TPs is expected in the case of anisotropic or uniaxial σ . This expectation is discussed in the following subsection. Snapshots of u obtained on the fluid lattice are shown in Figs. 7(a)–7(d), where the parameters are the same as those for the fixed model in Fig. 6 except for $D_v = 10$, which is twice as large as that in Fig. 6. If $D_v = 5$ is used for the fluid model, then some of the patterns in Fig. 7 do not appear. This difference is considered to come from a difference in the lattice structure between fixed and fluid lattices. The vertex positions \vec{r} on fluid lattices are expected to be more influenced

by the external force \vec{F} and their nearest neighbors via the correlation energy $S_{\vec{\tau}}$ due to the free diffusion of vertices shown in Fig. 19(c). To see such a difference in the lattice structure, we calculate the direction-dependent diffusion constants in the following subsection (Appendix F) and the distribution $h(\ell)$ of the bond length ℓ in Appendix G.

B. Direction-dependent diffusion constants and surface tension

In Figs. 8(a) and 8(b), we plot direction-dependent diffusion constants (Appendix F)

$$D_u^x = \frac{1}{N_B} \sum_{ij} \gamma_{ij}^u \cos^2 \theta_{ij}, \quad D_u^y = \frac{1}{N_B} \sum_{ij} \gamma_{ij}^u \sin^2 \theta_{ij},$$

$$D_v^x = \frac{1}{N_B} \sum_{ij} \gamma_{ij}^v \cos^2 \theta_{ij}, \quad D_v^y = \frac{1}{N_B} \sum_{ij} \gamma_{ij}^v \sin^2 \theta_{ij}, \quad (17)$$

and the corresponding direction-dependent energies

$$S_u^x = \frac{\sum_{ij} \gamma_{ij}^u \cos^2 \theta_{ij} (u_i - u_j)^2}{(1/N_B) \sum_{ij} \gamma_{ij}^u \cos^2 \theta_{ij}},$$

$$S_u^y = \frac{\sum_{ij} \gamma_{ij}^u \sin^2 \theta_{ij} (u_i - u_j)^2}{(1/N_B) \sum_{ij} \gamma_{ij}^u \sin^2 \theta_{ij}},$$

$$S_v^x = \frac{\sum_{ij} \gamma_{ij}^v \cos^2 \theta_{ij} (v_i - v_j)^2}{(1/N_B) \sum_{ij} \gamma_{ij}^v \cos^2 \theta_{ij}},$$

$$S_v^y = \frac{\sum_{ij} \gamma_{ij}^v \sin^2 \theta_{ij} (v_i - v_j)^2}{(1/N_B) \sum_{ij} \gamma_{ij}^v \sin^2 \theta_{ij}}, \quad (18)$$

where $N_B (= 3N)$ is the total number of bonds and θ_{ij} is the angle between \vec{e}_{ij} and the x axis (Fig. 21). We calculate these quantities using the final configurations obtained in step (iv) described in Sec. III B. The final configurations of u , v , and

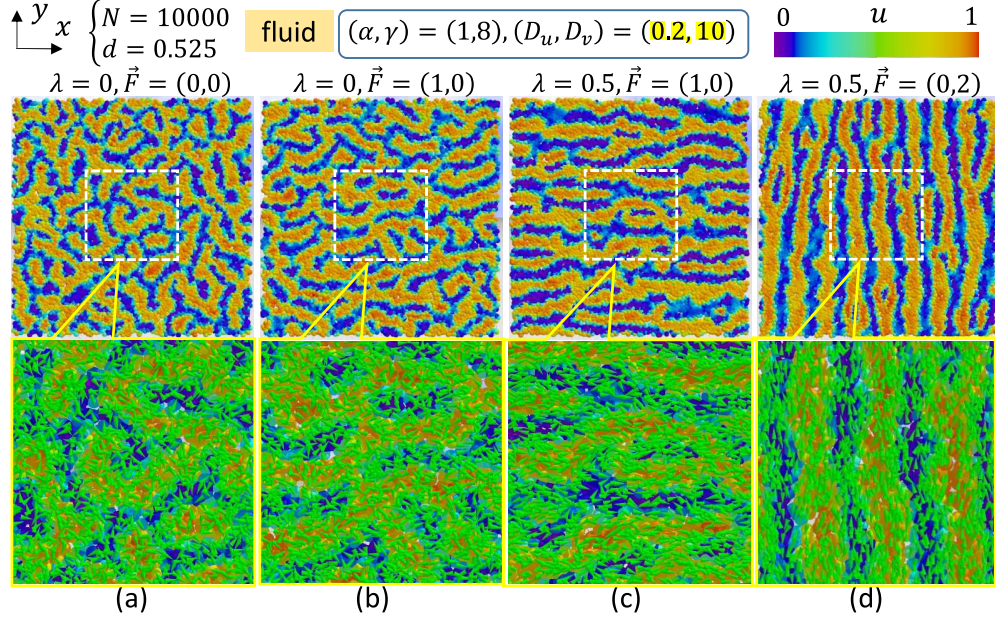


FIG. 7. Snapshots of TPs for u obtained on the fluid lattice of size $N = 10\,000$ with lattice spacing $d = 0.525$. The assumed parameters are shown in the figure. These are the same as those assumed in Fig. 6 except for $D_v = 10$.

$\bar{\tau}$ depend on their initial configurations, and for this reason, we obtain their mean final values by repeating steps (i) to (iv) n_{itr} times with random initial configurations as described in step (v). This mean value corresponds to the ensemble average in the statistical mechanical sense. n_{itr} , the total number of iterations n_{MC} of steps (i) and (ii), and the lattice size N for the simulations in this subsection are assumed to be as follows:

$$n_{\text{itr}} = 50, \quad n_{\text{MC}} = 5 \times 10^5, \quad N = 6400. \quad (19)$$

Open and solid symbols plotted in Fig. 8(a) correspond to the data obtained on the lattices of lattice spacings $d = 0.525$ and $d = 0.41$, respectively, and the data are almost independent of d . This independence of d , observed in $D_{u,v}^\mu$, implies that anisotropic TPs are not influenced by the difference of $\sigma(\propto d^{-2})$ originated in d . We also find that D_u^x (D_u^y) increases (decreases) with increasing F . Note that the IDOF $\bar{\tau}$ is almost random as $F \rightarrow 0$ and aligns along the x axis when F increases. This behavior of D_u^x and D_u^y is consistent with that of $D_u^x = aD_u$ and $D_u^y = (2 - a)D_u$ expected when a in Eq. (3) in the preceding section increases from $a = 1$. Moreover, we find that S_u^x/N_B (S_u^y/N_B) decreases (increases) with increasing F .

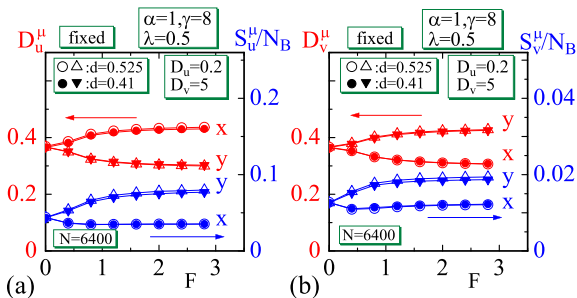


FIG. 8. (a) D_u^μ and S_u^μ vs F [$\vec{F} = (F, 0)$], and (b) D_v^μ and S_v^μ vs F for the fixed model on a lattice of size $N = 6400$.

Here we note that S_u^μ/N_B and D_u^μ have no relationship between the input and output, but both S_u^μ/N_B and D_u^μ are outputs to the input F . To compare the results plotted in Figs. 8(a) and 8(b) with those in Figs. 4(a) and 4(b), we consider the results in Figs. 8(a) and 8(b) as the “responses” S_u^μ and S_v^μ to the “inputs” D_u^μ and D_v^μ as follows:

$$\text{Fig. 8(a): } S_u^x \searrow \text{ (if } D_u^x \nearrow \text{), } S_u^y \nearrow \text{ (if } D_u^y \searrow \text{),} \quad (20)$$

$$\text{Fig. 8(b): } S_v^x \searrow \text{ (if } D_v^x \searrow \text{), } S_v^y \nearrow \text{ (if } D_v^y \nearrow \text{).} \quad (21)$$

Thus, we find that the results in Eqs. (20) and (21) are consistent with the behaviors of $|\partial_\mu^2 u|$ and $|\partial_\mu^2 v|$ vs a and b in Figs. 4(a) and 4(b). Notably, the relation in terms of increases or decreases between S_v^μ and D_v^μ is opposite to that between S_u^μ and D_u^μ . This consistency of Eqs. (20) and (21) and Fig. 5 with Eq. (3) implies that the FG modeling with the IDOF $\bar{\tau}$ suitably implements the diffusion anisotropy in TPs. The same consistency is obtained with the results on the fluid lattice plotted in Figs. 9(a) and 9(b).

Next, we show the surface tension σ in Eq. (E5) for the lattice spacings $d = 0.525$ and $d = 0.41$ in Figs. 10(a) and

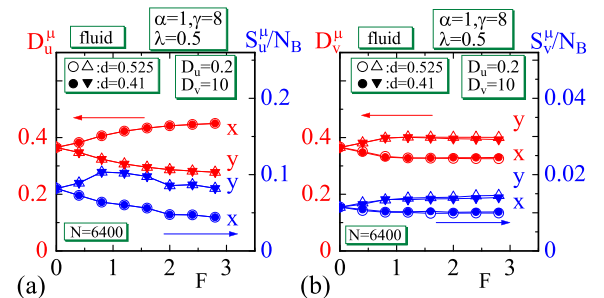


FIG. 9. (a) D_u^μ and S_u^μ vs F [$\vec{F} = (F, 0)$] and (b) D_v^μ and S_v^μ vs F for the fluid model on a lattice of size $N = 6400$.

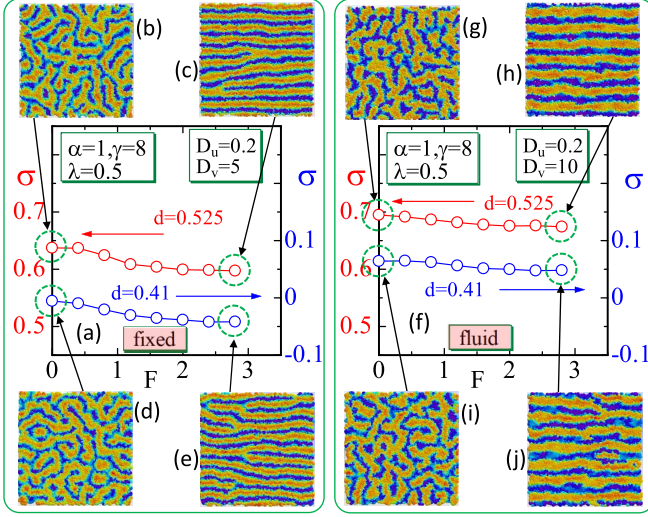


FIG. 10. Surface tension σ vs F [$\vec{F} = (F, 0)$] on the (a) fixed lattice, with (b)–(e) snapshots of u at $F = 0$ and $F = 2.8$, and on the (f) fluid lattice, with (g)–(j) snapshots of u at $F = 0$ and $F = 2.8$, where the lattice spacing is assumed to be $d = 0.525$ and $d = 0.41$. The lattice size ($N = 6400$) and the parameters are the same as those assumed in Figs. 8 and 9. We find that $\sigma(d = 0.525) > 0$ and $\sigma(d = 0.41) \simeq 0$, and both of them decrease with increasing F .

10(b). We have checked that the patterns are not influenced by the difference in $\sigma(\propto d^{-2})$ in Figs. 8 and 9; however, observing the interaction between σ and IDOF $\vec{\tau}$, which is controlled by the external force \vec{F} , is still interesting. We find from Figs. 10(a) and 10(b) that $\sigma(d = 0.525) > 0$ and $\sigma(d = 0.41) \simeq 0$ as expected, and moreover, σ slightly decreases as F increases in both the fixed and fluid lattices. This dependence of σ on F implies that σ depends on IDOF $\vec{\tau}$ because F directly influences $\vec{\tau}$, and therefore we consider that $\vec{\tau}$ interacts with σ . This interaction between $\vec{\tau}$ and σ allows us to control $\vec{\tau}$ with σ through an anisotropic frame or boundary condition. This prediction is confirmed in the following subsection.

C. Control of the pattern direction

First, we show that the pattern direction can be arbitrarily and spontaneously determined. The snapshots in Fig. 11(a) denoted by “forced” are obtained with $\vec{F} = (3, 3)$ and $\lambda = 0$. In this case, the direction of IDOF $\vec{\tau}$ is controlled by \vec{F} , and consequently, patterns align along $\vec{\tau}$. In contrast, the snapshots in Fig. 11(b) denoted by “spontaneous” are obtained under $\vec{F} = (0, 0)$ and $\lambda = 3$. In this case, IDOF $\vec{\tau}$ aligns along a spontaneously determined direction due to the relatively large $\lambda(\lambda=3)$; the pattern direction depends on random numbers for initial random configurations of $\vec{\tau}$. The snapshots in Fig. 11(c) are obtained by “forcing” with $\vec{F} = (3, 3)$, the same as in Fig. 11(a); however, the pattern direction is almost perpendicular to that in Fig. 11(a). The reason is that χ_{ij}^u in Eq. (B2) is replaced by χ_{ij}^v such that $\chi_{ij}^v = |\vec{\tau}_i \cdot \vec{e}_{ij}| + \chi_0$ and $\chi_{ij}^u = \sqrt{1 - |\vec{\tau}_i \cdot \vec{e}_{ij}|^2} + \chi_0$ (Appendix B). These properties of the pattern direction, forced, spontaneous, and $\chi_{ij}^{u,v}$ dependent, are specific to FG models. Now we deform the

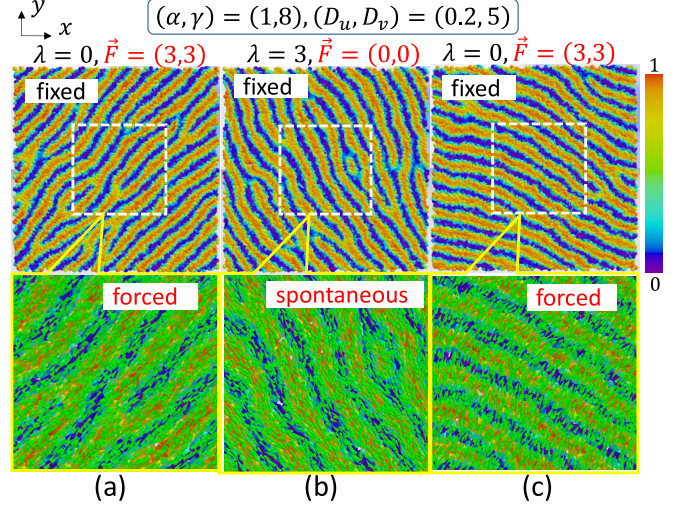


FIG. 11. Snapshots of TPs for u , the direction of which is (a) “forced” by external \vec{F} and (b) spontaneously determined without \vec{F} . The central domains are plotted with small cones representing IDOF $\vec{\tau}$ in the lower part. (c) “Forcing” with the replacement of $\chi_{ij}^u \leftrightarrow \chi_{ij}^v$ in Eq. (B2), where the pattern direction is vertical to IDOF $\vec{\tau}$.

side lengths L_x and $L_y(=L_x)$ of the lattice using the parameter R_{XY} such that $L'_x = L_x/\sqrt{R_{XY}}$ and $L'_y = \sqrt{R_{XY}}L_y$, where $R_{XY} = L'_y/L'_x$, without changing the area [$L'_{x,y}$ are written as $L_{x,y}$ in Figs. 12(a)–12(c)].

Snapshots of lattices deformed within the range $0.6 \leq R_{XY} \leq 1.4$ of the fixed model are shown in Figs. 13(a)–13(b). The TP direction aligns along the longer direction when the ratio R_{XY} deviates from $R_{XY} = 1$ to a certain extent. The parameters are shown in the figure. We find that IDOF $\vec{\tau}$ aligns along the longer direction, along which bond lengths are longer than those along the shorter direction, as observed in Figs. 12(a) and 12(c). This observation indicates that vertices fluctuate along the longer direction relatively easily compared to the vertical direction. This is the alignment mechanism of anisotropic TPs due to the boundary condition. We note that the lattice deformation is caused by uniaxial tensile strain or compression, and therefore, we consider that mechanical anisotropic strain applied on the boundary imparts TP anisotropy.

On fluid lattices, this mechanism does not work because vertices freely move due to their fluid nature. Nevertheless, even on fluid lattices, a fixed boundary condition can be assumed to prohibit vertices from undergoing free diffusion in the perpendicular direction. In this case, the direction of TPs is also expected to be determined by this fixed boundary condition [Figs. 14(a) and 14(b)]. We find from Figs. 15(a) and 15(b) that TPs align along the fixed-boundary direction on the fluid lattices.

Finally, we calculate the mean values of $D_u^\mu(\mu = x, y)$ corresponding to the snapshots in Figs. 13 and 15 using $n_{\text{itr}} = 50$ convergent configurations, which is the same number as in Eq. (19). We find from Fig. 16(a) that D_u^x (D_u^y) of the fixed model increases (decreases) with increasing R_{XY} , while D_u^x and D_u^y of the fluid model are independent of R_{XY} . The obtained data $D_u^\mu(\mu = x, y)$ vs R_{XY} are consistent with those

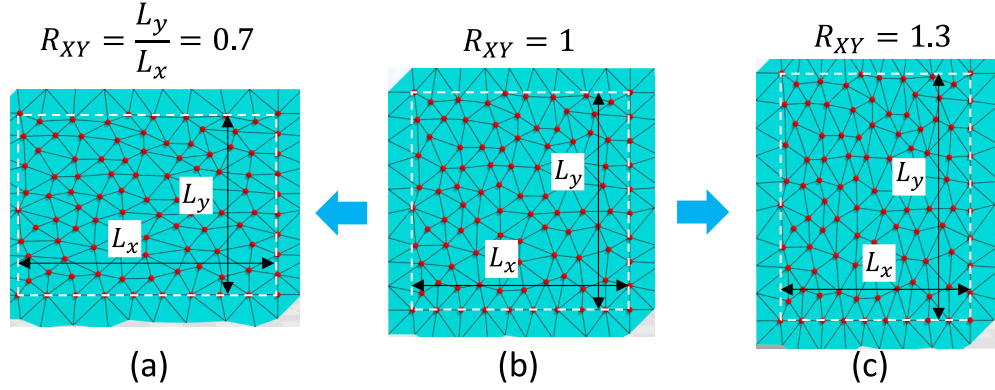


FIG. 12. Initial configurations of deformed and original lattices. The ratio of side lengths is (a) $R_{XY} = 0.7$, (b) $R_{XY} = 1$, and (c) $R_{XY} = 1.3$. The area $L_x L_y$ remains unchanged under deformation. A small lattice of size $N = 100$ is used for visualization of the lattice structure.

plotted in Figs. 8 and 9 corresponding to anisotropic TPs caused by external force $\vec{F} (\neq (0, 0))$. The “x-dir bnd” (“y-dir bnd”) symbols in Fig. 16(b) denote the fixed boundary in the x (y) direction shown in Figs. 14 and 15. The results that $D_u^x > D_u^y$ for “x-dir bnd” and $D_u^x < D_u^y$ for “y-dir bnd” within the range $1 \leq \lambda \leq 4$ are also consistent with the expectation from the pattern directions at $\lambda = 3$ in Figs. 15(a) and 15(b), respectively. No clear difference is observed between D_v^x and D_v^y (which are not plotted) compared to the cases for D_u^μ ($\mu = x, y$), although D_v^μ ($\mu = x, y$) exhibits the opposite behavior to D_u^μ ($\mu = x, y$) when $R_{XY} \geq 1.5$ or $R_{XY} \leq 0.6$ in the fixed model and $\lambda \geq 4$ in the fluid model.

Note that the lattice shape deformation (Fig. 13) causes direction-dependent anisotropic diffusion due to $\gamma_{ij}^{u,v}$ in the modified Laplacian in Eq. (11). This direction dependence of $\gamma_{ij}^{u,v}$ is caused by $\vec{\tau}$ alignment along the expanded lattice direction in the fixed model and/or along the fixed boundary direction in the fluid model. Moreover, the alignment of $\vec{\tau}$ is

closely connected to vertex movement owing to the effects of the Gaussian bond potential S_1 in Eq. (D2) in our modeling. Indeed, S_1 can influence vertex movement on anisotropically deformed lattices because S_1 is introduced to make the surface isotropic in-plane mechanically. Thus, the $\vec{\tau}$ alignment implies that the microscopic and direction-dependent fluctuation of lipid molecules in membranes is a possible origin of anisotropic TPs (Fig. 1).

V. CONCLUDING REMARKS

In this paper, we have shown that the FG modeling technique is applicable to a differential equation model called the RD equation of FitzHugh-Nagumo for TPs. This FG modeling scheme dynamically implements anisotropy in the diffusion coefficients via an IDOF, which corresponds to direction-dependent fluctuations of lattice vertices, preserving the competing nature between the activator and inhibitor. The

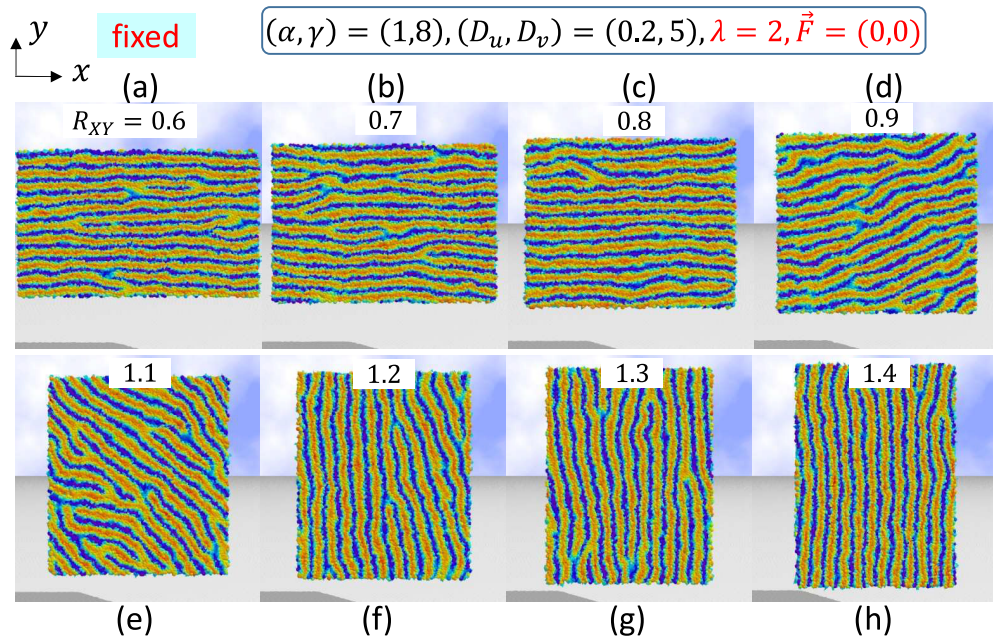


FIG. 13. Alignment of anisotropic TPs of u along the longer direction of lattices deformed with the ratio $R_{XY} = L_y/L_x$ ranging from (a) $R_{XY} = 0.6$ to (h) $R_{XY} = 1.4$. These alignments are caused by strains applied on the boundary frame of lattices.

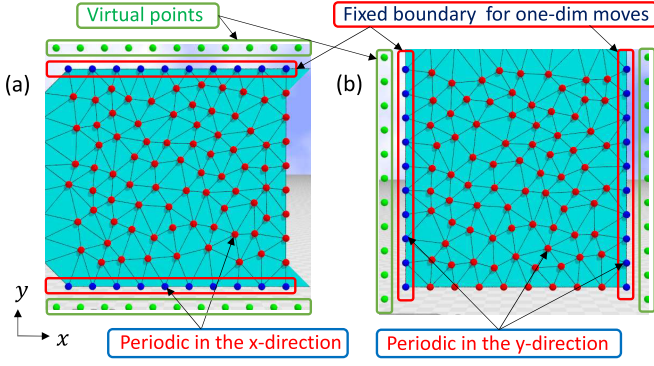


FIG. 14. A PBC or the fluid model is assumed in (a) the x direction for vertices in red (●) and blue (●), denoted by “Fixed boundary for one-dim moves” along the boundary. The vertices (●) outside the fixed boundaries are “virtual points” used to define $\gamma_{ij}^{u,v}$ in Eq. (D2) on the boundaries. (b) A PBC is assumed in the y direction. The lattice size is $N = 100$, in which the virtual points are not included.

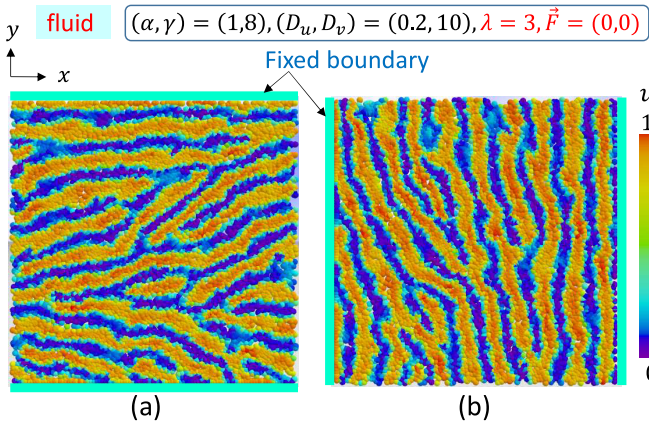


FIG. 15. Snapshots of u obtained on fluid lattices, in which a pair of fixed boundaries is assumed in (a) the x direction and (b) the y direction. The lattice size is $N = 10000$, and the parameters are shown in the figure. The alignment of TPs and their directions are determined by the boundary conditions.

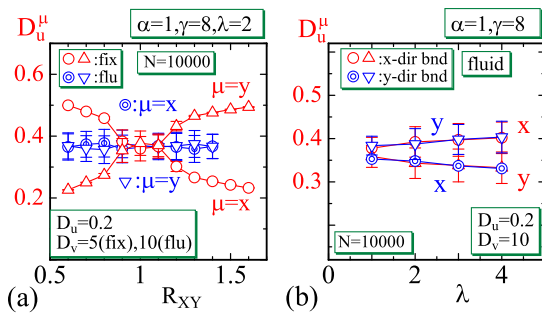


FIG. 16. (a) D_u^μ , ($\mu = x, y$) vs R_{XY} of fixed and fluid models, and (b) D_u^μ , ($\mu = x, y$) vs λ of the fluid model with fixed boundary conditions denoted by “ x -dir bnd” and “ y -dir bnd.” The error bars denote the standard deviation. The behavior of D_u^μ is consistent with the anisotropic TPs shown in the snapshots in Figs. 13 and 15.

IDOF on fixed-connectivity lattices is controlled by uniaxial strains corresponding to frame or surface tensions, which are anisotropically imposed by boundary conditions.

The lattice vertices are biologically interpreted as cells or lumps of cells, and animal cells are activated by molecular motors and strongly influenced by thermal fluctuations of lipid molecules. For these reasons, considering that cell movements accompany fluctuations is natural. Therefore, the FG modeling indicates that one possible origin of anisotropic TPs is direction-dependent fluctuations of cells.

We confirm that the TP direction is controlled by the surface boundary conditions such that the direction aligns along the tensile or compressive strain direction on fixed-connectivity lattices. On fluid lattices with a pair of fixed boundaries, we confirm that TPs can also be controlled to anisotropically emerge along the direction of the fixed boundaries.

ACKNOWLEDGMENTS

This work is supported in part by Collaborative Research Project No. J22Ly19 of the Institute of Fluid Science (IFS), Tohoku University. The authors acknowledge Jean-Paul Rieu and Benjamin Ducharme for suggestions. The author H.K. acknowledges Roland Denis, Elie Bretin, Simon Masnou and Camille Carvalho for discussions. Numerical simulations were performed on the supercomputer system AFI-NITY at the Advanced Fluid Information Research Center, Institute of Fluid Science, Tohoku University.

APPENDIX A: INTERNAL DEGREE OF FREEDOM ON THE TRIANGULATED LATTICE AND THE MONTE CARLO UPDATE

First, we present detailed information on triangulated lattices in which the vertex position plays a role in the IDOF for anisotropic diffusion. This new IDOF is governed by the Hamiltonian S in Eq. (12). A triangulated lattice is illustrated in Fig. 17, where PBCs are assumed for all vertex positions. In the initial configuration shown in Fig. 17, the vertices enclosed by the solid rectangles are identified with those enclosed by the same-sized oblong dashed rectangles, which are plotted at positions $n_\mu d$, ($\mu = x, y$) distant from the original positions, where n_μ and d represent the total number of vertices on the lattice edges and the lattice spacing, respectively. The dashed square represents a frame implemented by PBCs, in which the vertex position \vec{r} is identified with $\vec{r} \pm (n_x d, n_y d)$ such that $\vec{r} \equiv \vec{r} \pm (n_x d, n_y d)$. Consequently, the frame area is fixed to $A = L_x L_y$, where L_μ ($\mu = x, y$) is the edge length given by $L_\mu = (n_\mu - 1)d$. Vertices on and inside the dashed frame in Fig. 17 representing the initial configuration are linked with the Voronoi tessellation technique [37]. Next, to introduce an IDOF, we briefly explain the MC update [38,39] of the vertex position $\vec{r} \in \mathbf{R}^2$, which is illustrated in Fig. 18(a). The new position \vec{r}' is accepted with a probability $\text{Min}[1, \exp(-\delta S)]$, where $\delta S = S(\vec{r}') - S(\vec{r})$ is the energy change after the vertex movement $\vec{r} \rightarrow \vec{r}'$. The new position \vec{r}' is randomly fixed in a small circle of radius R centered at \vec{r} , where the radius R is fixed such that the acceptance rate is approximately equal to 60–90% under the constraint

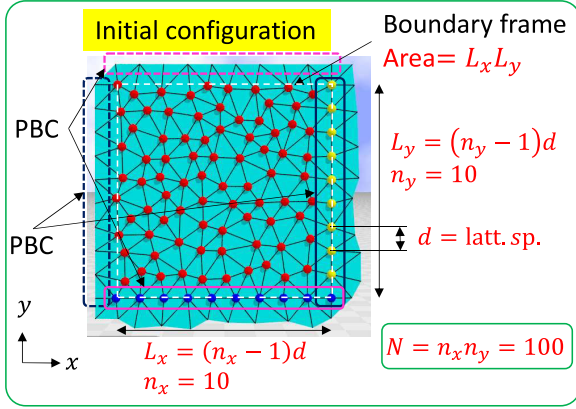


FIG. 17. Triangulated square lattice of size $N = 100$, which is the total number of vertices given by $N = n_x n_y$, where the total number of boundary vertices is $n_\mu = 10 (\mu = x, y)$. The edge length $L_\mu (\mu = x, y)$ is given by $L_\mu = (n_\mu - 1)d$, where d is the lattice spacing. PBCs are assumed at the boundary vertices. The dashed square is the boundary frame of area $A = L_x L_y$ implemented by the PBCs.

that the triangles are not folded at any bond [nonfolding and folding triangles are illustrated in Fig. 18(c)]. This MC process for the update of vertex positions is the same as that in MC studies for polymerized membranes [40–42], which is a two-dimensional extension of the linear chain model for polymers [43]. Another MC process is the bond flip procedure shown in Fig. 18(b) [44]. In this process, bond ij connecting vertices i and j is removed, and vertices k and l are connected by a bond. This bond flip is also accepted with probability $\text{Min}[1, \exp(-\delta S)]$ with energy change δS under the constraint of nonfolding triangles. The IDOF $\bar{\tau}$ is defined by

$$\bar{\tau} = \frac{\Delta \vec{r}}{\|\Delta \vec{r}\|} \quad (\in S^1/2) \quad (\text{A1})$$

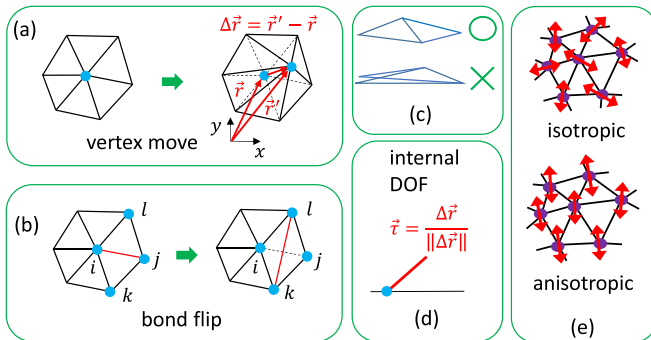


FIG. 18. Illustrations of MC updates for (a) the vertex position and (b) bond flip under the constraint of nonfolding triangles. Lattices in which only the vertex position is updated are called fixed-connectivity lattices, and those in which both the vertex position and bond flip are updated are called fluid lattices. (c) Triangles are allowed to deform in non-folding configurations (O) and are prohibited from folding (X). (d) The IDOF $\bar{\tau} (\in S^1/2)$ at \vec{r} is defined by $\bar{\tau} = \Delta \vec{r} / \|\Delta \vec{r}\|$ using the deformation vector $\Delta \vec{r} = \vec{r}' - \vec{r}$. (e) Illustrations of vertex fluctuations corresponding to isotropic and anisotropic configurations of $\bar{\tau}$.

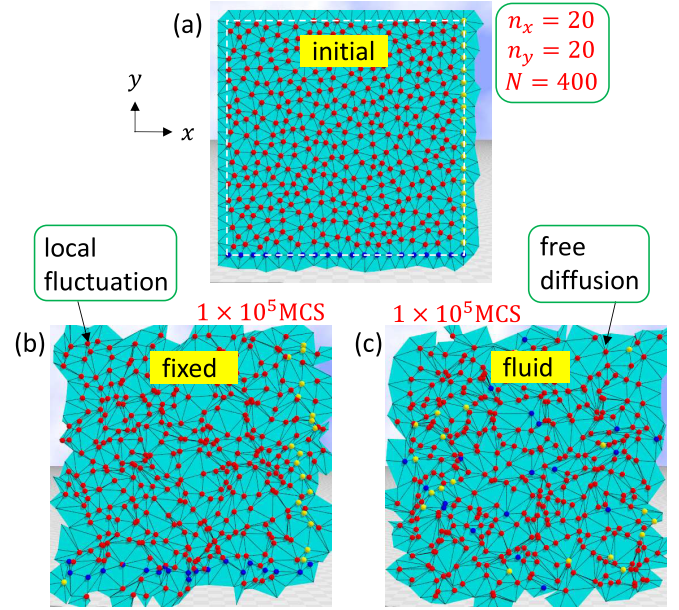


FIG. 19. Snapshots of vertex configurations updated by the Metropolis MC procedure with lattice size $N = 400$: (a) initial configuration without the MC update, (b) fixed connectivity lattice obtained after 1×10^5 MC sweeps (MCS) for the vertex updates, and (c) fluid lattice obtained after 1×10^5 MCS for the vertex and bond flip updates. The vertices on the boundaries of the fixed lattice in (b) fluctuate only locally, whereas those of the fluid lattice in (c) diffuse over the lattice. The total number of bonds N_B and total number of triangles N_T are given by $N_B = 3N$ and $N_T = 2N$ on triangulated lattices with PBCs satisfying zero Euler characteristics $N - N_B + N_T = 0$.

[Fig. 18(d)], which has values on the half circle $S^1/2$ due to the nonpolar nature assumed for the variable. Figure 18(e) shows the isotropic and anisotropic configurations of $\bar{\tau}$. Finally, in this Appendix, we present snapshots of vertex configurations updated by the MC process, including the initial configuration [Fig. 19(a)]. To clearly show the vertices, we use a small lattice of size $N = 400$. A snapshot denoted by “fixed” in Fig. 19(b) is obtained after 1×10^5 MC sweeps (MCS) for the update of vertex position \vec{r}_i only, where 1 MCS represents N consecutive updates of \vec{r}_i , ($i = 1, \dots, N$). Vertices outside the dashed square shown in Fig. 19(a) are plotted on the opposite side due to the PBC. We find that the vertices fluctuate only locally on the fixed connectivity lattice. In contrast, the vertices diffuse almost freely over the lattice denoted by “fluid” in Fig. 19(c) [44,45]; we find that the boundary vertices are randomly mixed on the fluid lattice, where 1 MCS represents N consecutive updates of vertex positions followed by N random updates of bond flips.

We emphasize that these two different types of triangulated lattices are not simply different in polygon shape from the regular square lattice in Sec. II but rather have extra dynamic degrees of freedom, such as the vertex position. To suitably treat this new IDOF, we introduce the Gaussian bond potential, which is usually assumed for a cell membrane model [45–47], in the Hamiltonian S of Eq. (12).

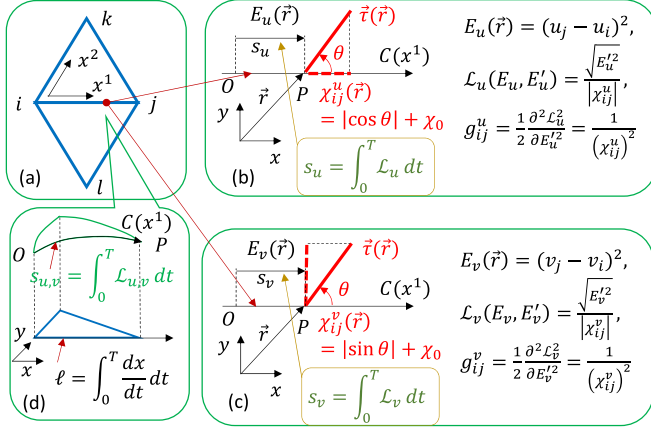


FIG. 20. (a) Local coordinate system (x^1, x^2) with the origin at vertex i on a triangle Δ_{ijk} , (b) unit Finsler length χ_{ij}^u for the diffusion anisotropy of u on the curve $C(x^1)$ along the x^1 axis, (c) unit Finsler length χ_{ij}^v corresponding to the variable v , and (d) intuitive illustrations of Euclidean length ℓ and Finsler length $s_{u,v}$ between O and P along the x^1 and $C(x^1)$ axes, respectively. The direction-dependent Finsler metrics g^u and g^v along the x^1 axis, which is assumed to be parallel to the x axis, from i to j are obtained by using Finsler functions \mathcal{L}_u and \mathcal{L}_v such that $g^u = 1/(\chi_{ij}^u)^2$ and $g^v = 1/(\chi_{ij}^v)^2$. Arrows with x and y in (b), (c), and (d) represent the canonical coordinate axes of \mathbf{R}^2 .

APPENDIX B: FINSLER FUNCTION AND FINSLER LENGTH

In this Appendix, we introduce technical details of Finsler metrics for diffusion anisotropy. The Finsler length can be introduced in a local coordinate system (x^1, x^2) on triangulated lattices in a discrete manner [Fig. 20(a)]. The origin of the local coordinate is the vertex position i of the triangle Δ_{ijk} . The x^1 axis is considered a curve $C(x^1)$, on which a Finsler function \mathcal{L} is introduced using a coordinate function $E_u(\vec{r}) = E_u(x^1)$ and its first derivative $E'_u(x^1) = \frac{dE_u}{dx^1}$:

$$\mathcal{L}_u(E_u, E'_u) = \frac{\sqrt{E_u'^2}}{|\chi^u|},$$

$$E_u = \int_0^{x^1} \left(\frac{\partial u}{\partial x^1} \right)^2 dx^1, \quad E'_u = \frac{dE_u}{dx^1}. \quad (\text{B1})$$

Here we use the expression $(\frac{\partial u}{\partial x^1})^2 = (\nabla u)^2$ along $C(x^1)$. $E_u(x^1)$ is an energy function that is positive, increases with increasing $(\nabla u)^2$ along the x^1 axis, and monotonically increases with respect to x^1 ; hence, $E_u(x^1)$ can be used to define the Finsler length along $C(x^1)$. Note that this coordinate function $E_u(\vec{r}) = E_u(x^1)$ differs from that in Ref. [27], where an induced metric is used, and hence, the coordinate functions are defined on the tangential lines of the Euclidean length on curved surfaces. From the general prescription, we obtain the Finsler length s by time integration of the Finsler function \mathcal{L} along $C(x^1)$ from $t = 0$ to $t = T$: $s = \int_0^T \mathcal{L}(E_u, E'_u) dt$. Equivalently, we obtain the corresponding Finsler metric

element g^u along the x^1 axis, $g^u = (1/2)\partial^2 \mathcal{L}_u^2 / \partial E_u'^2 = 1/(\chi_{ij}^u)^2$, which is suitable for our purpose. Another Finsler metric for the anisotropic diffusion of variable v along $C(x^1)$ can also be obtained using $g^v = (1/2)\partial^2 \mathcal{L}_v^2 / \partial E_v'^2 = 1/(\chi_{ij}^v)^2$. Here we assume that χ_{ij}^u and χ_{ij}^v are given by

$$\chi_{ij}^u = |\vec{\tau}_i \cdot \vec{e}_{ij}| + \chi_0, \quad \chi_{ij}^v = \sqrt{1 - |\vec{\tau}_i \cdot \vec{e}_{ij}|^2} + \chi_0, \quad (\text{B2})$$

where $\vec{\tau}_i$ denotes the IDOF at vertex i , \vec{e}_{ij} denotes the unit tangential vector from vertices i to j , and χ_0 denotes a small positive number. These parameters χ_{ij}^u and χ_{ij}^v on $C(x^1)$ are visualized by the dashed lines in Figs. 20(b) and 20(c).

Here we note that the relation of the Euclidean length dx^1 between i and j with the Finsler length ds_u from i to j is given by using the Finsler metric g^u : $(ds_u)^2 = g^u(dx^1)^2 = (dx^1)^2/(\chi_{ij}^u)^2$. Thus, we have that $ds_u = dx^1/\chi_{ij}^u$, and therefore, $ds_u = 1$ for $dx^1 = \chi_{ij}^u$. Therefore, we call χ_{ij}^u the unit Finsler length from i to j . We sometimes call χ_{ij}^u a ‘‘velocity,’’ as χ_{ij}^u physically has units of velocity because the Finsler length ds_u is a time length. Along the x^2 axis from vertices i to k in Fig. 20(a), the unit Finsler lengths χ_{ik}^u and χ_{ik}^v can be defined by replacing \vec{e}_{ij} with \vec{e}_{ik} in Eq. (B2). Thus, we obtain the two-dimensional Finsler metrics g^u and g^v with respect to the local coordinate (x^1, x^2) :

$$g^u = \begin{bmatrix} 1/(\chi_{ij}^u)^2 & 0 \\ 0 & 1/(\chi_{ik}^u)^2 \end{bmatrix}, \quad g^v = \begin{bmatrix} 1/(\chi_{ij}^v)^2 & 0 \\ 0 & 1/(\chi_{ik}^v)^2 \end{bmatrix}. \quad (\text{B3})$$

APPENDIX C: DISCRETE HAMILTONIAN FOR THE MODIFIED LAPLACIAN

Using g^u in Eq. (B3), we show the outline of discretization of S_u in S of Eq. (12) from the continuous Hamiltonian

$$S_u = \frac{1}{2} \int \sqrt{g^u} d^2x g_u^{ab} \frac{\partial u}{\partial x^a} \frac{\partial u}{\partial x^b}. \quad (\text{C1})$$

The integral is replaced by the sum of the triangles with the determinant $g = \det(g^u)$, i.e., $\int \sqrt{g^u} d^2x \rightarrow \sum_{\Delta} 1/(\chi_{ij}^u \chi_{ik}^u)$, and the differentials are replaced by differences with the inverse metric $g_u^{ab} = (g^u)^{-1}$, i.e., $g_u^{ab} \frac{\partial u}{\partial x^a} \frac{\partial u}{\partial x^b} = g_u^{11} (\frac{\partial u}{\partial x^1})^2 + g_u^{22} (\frac{\partial u}{\partial x^2})^2 \rightarrow (\chi_{ij}^u)^2 (u_j - u_i)^2 + (\chi_{ik}^u)^2 (u_k - u_i)^2$. Thus, we have $S_u = \frac{1}{2} \int \sqrt{g^u} d^2x g_u^{ab} \frac{\partial u}{\partial x^a} \frac{\partial u}{\partial x^b} \rightarrow \frac{1}{2} \sum_{\Delta} [\frac{\chi_{ij}^u}{\chi_{ik}^u} (u_j - u_i)^2 + \frac{\chi_{ik}^u}{\chi_{ij}^u} (u_k - u_i)^2]$. Here we note that there are two different origins of the local coordinates at vertices j and k other than that at i on triangle Δ_{ijk} [Fig. 20(a)]. The discrete expressions of S_u corresponding to these local coordinates on Δ_{ijk} are obtained by replacing the indices $ijk \rightarrow jki$ and $jki \rightarrow kij$ and summing over three different expressions with a factor

1/3, and we obtain

$$\begin{aligned}
 S_u &= \frac{1}{6} \sum_{\Delta_{ijk}} \left[\frac{\chi_{ij}^u}{\chi_{ik}^u} (u_j - u_i)^2 + \frac{\chi_{ik}^u}{\chi_{ij}^u} (u_k - u_i)^2 + \frac{\chi_{jk}^u}{\chi_{ji}^u} (u_k - u_j)^2 + \frac{\chi_{ji}^u}{\chi_{jk}^u} (u_i - u_j)^2 + \frac{\chi_{ki}^u}{\chi_{kj}^u} (u_i - u_k)^2 + \frac{\chi_{kj}^u}{\chi_{ki}^u} (u_j - u_k)^2 \right] \\
 &= \sum_{\Delta_{ijk}} [\tilde{\gamma}_{ij}^u (u_i - u_j)^2 + \tilde{\gamma}_{jk}^u (u_j - u_k)^2 + \tilde{\gamma}_{ki}^u (u_k - u_i)^2], \\
 \tilde{\gamma}_{ij}^u &= \frac{1}{6} \left(\frac{\chi_{ij}^u}{\chi_{ik}^u} + \frac{\chi_{ji}^u}{\chi_{jk}^u} \right), \quad \tilde{\gamma}_{jk}^u = \frac{1}{6} \left(\frac{\chi_{jk}^u}{\chi_{ji}^u} + \frac{\chi_{kj}^u}{\chi_{ki}^u} \right), \quad \tilde{\gamma}_{ki}^u = \frac{1}{6} \left(\frac{\chi_{ki}^u}{\chi_{kj}^u} + \frac{\chi_{ik}^u}{\chi_{ij}^u} \right), \quad (C2)
 \end{aligned}$$

where the sum of the triangles is explicitly denoted by $\sum_{\Delta_{ijk}}$. The summation convention can also be changed from a sum over triangles to a sum over bonds \sum_{ij} . Recalling that bond ij is shared by two triangles Δ_{ijk} and Δ_{jil} [Fig. 20(a)], we have to include terms $\frac{1}{6}(\frac{\chi_{ij}^u}{\chi_{ik}^u} + \frac{\chi_{ji}^u}{\chi_{jk}^u})(u_i - u_j)^2$ from Δ_{ijk} and $\frac{1}{6}(\frac{\chi_{ji}^u}{\chi_{jk}^u} + \frac{\chi_{ij}^u}{\chi_{ik}^u})(u_j - u_i)^2$ from Δ_{jil} in the sum over bonds \sum_{ij} . Thus, we have

$$\begin{aligned}
 S_u &= \sum_{ij} \gamma_{ij}^u (u_i - u_j)^2, \\
 \gamma_{ij}^u &= \frac{1}{6} \left(\frac{\chi_{ij}^u}{\chi_{ik}^u} + \frac{\chi_{ji}^u}{\chi_{jk}^u} + \frac{\chi_{ij}^u}{\chi_{il}^u} + \frac{\chi_{ji}^u}{\chi_{jl}^u} \right), \quad \gamma_{ij}^u = \gamma_{ji}^u. \quad (C3)
 \end{aligned}$$

Now, we describe the outline of the discretization of the Laplace-Beltrami operator

$$\Delta = \frac{1}{\sqrt{g}} \frac{\partial}{\partial x^a} \left(\sqrt{g} g^{ab} \frac{\partial}{\partial x^b} \right) \quad (C4)$$

on triangulated lattices. Since this operator includes second-order differentials, we adopt an indirect discretization scheme based on the discrete Hamiltonian S_u in Eq. (C3). The continuous expression of Δu can be obtained by the variational technique $\delta S_u = 0$ for the continuous S_u in Eq. (C1):

$$\begin{aligned}
 S_u &= \frac{1}{2} \int \sqrt{g^u} d^2 x g_u^{ab} \frac{\partial u}{\partial x^a} \frac{\partial u}{\partial x^b} \rightarrow \\
 \Delta u &= \frac{1}{\sqrt{g^u}} \frac{\partial}{\partial x^a} \left(\sqrt{g^u} g_u^{ab} \frac{\partial u}{\partial x^b} \right). \quad (C5)
 \end{aligned}$$

Therefore, we obtain the discrete expression Δu_i from S_u in Eq. (C3) using the discrete variational technique $\delta S_u = 0$:

$$\begin{aligned}
 S_u &= \sum_{ij} \gamma_{ij}^u (u_i - u_j)^2 \rightarrow \\
 \Delta u_i &= -\frac{\partial}{\partial u_i} \sum_{jk} \gamma_{jk}^u (u_j - u_k)^2, \quad (C6)
 \end{aligned}$$

such that

$$\Delta u_i = 2 \left(\sum_{j(i)} \gamma_{ij}^u u_j - u_i \sum_{j(i)} \gamma_{ij}^u \right) = \sum_{j(i)} 2\gamma_{ij}^u (u_j - u_i), \quad (C7)$$

where $\sum_{j(i)}$ denotes the sum over vertices j connected to vertex i by bonds ij [Fig. 21(a)]. To perform this summation, we replace sum \sum_{jk} over bonds jk in Eq. (C6) with $\frac{1}{2} \sum_j \sum_{k(j)} (= \sum_{jk})$, where \sum_j and $\sum_{k(j)}$ are the sum over vertices j and the sum over vertices k , which are connected to j with bonds jk , respectively. The 1/2 factor appears because of the duplicated sums in $\sum_j \sum_{k(j)}$; the term with index $jk = 12$ ($\Leftrightarrow j = 1, k = 2$) appears twice in $\sum_j \sum_{k(j)}$, for example. Notably, $\sum_j \sum_{k(j)} = \sum_k \sum_{j(k)}$ because $\sum_{jk} = \sum_{kj}$. Thus, we have

$$\begin{aligned}
 \frac{\partial}{\partial u_i} \sum_{jk} \gamma_{jk}^u (u_j - u_k)^2 &= \frac{\partial}{\partial u_i} \sum_{jk} \gamma_{jk}^u (u_j^2 + u_k^2 - 2u_j u_k) \\
 &= \frac{1}{2} \sum_j \sum_{k(j)} \gamma_{jk}^u 2(u_j \delta_{ji} + u_k \delta_{ki} - \delta_{ij} u_k - u_j \delta_{ik}) \\
 &= \sum_j \sum_{k(j)} \gamma_{jk}^u u_j \delta_{ji} + \sum_j \sum_{k(j)} \gamma_{jk}^u u_k \delta_{ki} - \sum_j \sum_{k(j)} \gamma_{jk}^u \delta_{ij} u_k \\
 &\quad - \sum_j \sum_{k(j)} \gamma_{jk}^u u_j \delta_{ik}, \quad (C8)
 \end{aligned}$$

where δ_{ij} is the Kronecker delta. In this final expression, the first term is $\sum_j \sum_{k(j)} \gamma_{jk}^u u_j \delta_{ji} = \sum_{k(i)} \gamma_{ik}^u u_i = u_i \sum_{k(i)} \gamma_{ik}^u$, and the second term can be written as $\sum_j \sum_{k(j)} \gamma_{jk}^u u_k \delta_{ki} = \sum_k \sum_{j(k)} \gamma_{jk}^u u_k \delta_{ki} = \sum_{j(i)} \gamma_{ji}^u u_i = u_i \sum_{j(i)} \gamma_{ji}^u$, which is identical to the first term. The third term is $-\sum_j \sum_{k(j)} \gamma_{jk}^u \delta_{ij} u_k = -\sum_{k(i)} \gamma_{ik}^u u_k$, which is identical to the fourth term $-\sum_j \sum_{k(j)} \gamma_{jk}^u u_j \delta_{ik} = -\sum_k \sum_{j(k)} \gamma_{jk}^u u_j \delta_{ik} = -\sum_{j(i)} \gamma_{ji}^u u_j = -\sum_{j(i)} \gamma_{ij}^u u_j$. This proves Eq. (C7).

Here we comment on the relation between Δ in Eq. (C7) and the network Laplacian $\sum_{j=1}^N L_{ij} u_j = \sum_{j=1}^N A_{ij} (u_j - u_i)$,

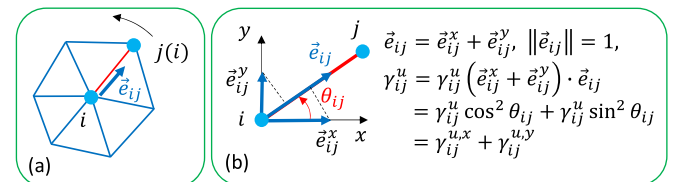


FIG. 21. (a) Vertices $j(i)$ connected to vertex i and (b) unit tangential vector \vec{e}_{ij} from vertex i to vertices $j(i)$ and its decomposition into the canonical coordinate axis components.

where N is the total number of nodes (or vertices) and $L_{ij} = A_{ij} - k_i \delta_{ij}$, with $k_i = \sum_{j=1}^N A_{ij}$. The adjacency (or connectivity) matrix A_{ij} is defined as $A_{ij} = 1$ if i and j are connected and $A_{ij} = 0$ otherwise. Rewriting Δu_i in Eq. (C7) as

$$\Delta u_i = \sum_{ij} 2\gamma_{ij}^u (A_{ij} - k_i \delta_{ij}), \quad (\text{C9})$$

we find that Δu_i is a weighted network Laplacian with weight $2\gamma_{ij}^u$. Note that γ_{ij}^u is well defined for networks on

The Hamiltonian S in Eq. (12) is as follows:

$$S(\vec{r}; \vec{\tau}) = \begin{cases} \gamma S_1 + U_V + D_u S_u + D_v S_v + \lambda S_\tau + S_\tau^F, & (\gamma = 1), \quad (\text{fixed}) \\ \gamma S_1 + U_V + U_{\mathcal{G}} + D_u S_u + D_v S_v + \lambda S_\tau + S_\tau^F, & (\gamma = 1), \quad (\text{fluid}), \end{cases} \quad (\text{D1})$$

and the terms on the right-hand side are

$$\begin{aligned} S_1 &= \sum_{ij} \ell_{ij}^2, & \ell_{ij}^2 &= (\vec{r}_i - \vec{r}_j)^2, \\ U_V &= \sum_{ij} U_{ij}, & U_{ij} &= \begin{cases} 0 & (\ell_{\min} \leq \ell_{ij} \leq \ell_{\max}) \\ \infty & (\text{otherwise}) \end{cases}, \\ (\ell_{\min} &= 0.01d \quad \ell_{\max} = 3d, \quad d : \text{latt. sp.}), \\ U_{\mathcal{G}} &= \sum_i U_i, & U_i &= \begin{cases} 0 & (4 \leq q_i \leq 9) \\ \infty & (\text{otherwise}) \end{cases}, \\ S_u &= \sum_{ij} \gamma_{ij}^u (u_j - u_i)^2, & \gamma_{ij}^u &= \frac{1}{6} \left(\frac{\chi_{ij}^u}{\chi_{ik}^u} + \frac{\chi_{ji}^u}{\chi_{jk}^u} + \frac{\chi_{ij}^u}{\chi_{il}^u} + \frac{\chi_{ji}^u}{\chi_{jl}^u} \right), \\ S_v &= \sum_{ij} \gamma_{ij}^v (v_j - v_i)^2, & \gamma_{ij}^v &= \frac{1}{6} \left(\frac{\chi_{ij}^v}{\chi_{ik}^v} + \frac{\chi_{ji}^v}{\chi_{jk}^v} + \frac{\chi_{ij}^v}{\chi_{il}^v} + \frac{\chi_{ji}^v}{\chi_{jl}^v} \right), \\ S_\tau &= - \sum_{ij} (\vec{\tau}_i \cdot \vec{\tau}_j)^2, & S_\tau^F &= - \sum_i (\vec{\tau}_i \cdot \vec{F})^2, \quad \vec{F} = (F_x, F_y). \end{aligned} \quad (\text{D2})$$

The first term S_1 is the Gaussian bond potential, which is the spring potential defined by the sum of squared bond lengths ℓ_{ij}^2 . The inclusion of S_1 in S implies that domain \mathcal{D} is regarded as a membrane surface with an internal structure rather than a plane in \mathbf{R}^2 [40–42,44–47]. Therefore, we consider that the frame is spanned by a membrane of area $A = L_x L_y$ with surface tension σ , as mentioned in Appendix A (Appendix E for detailed information on σ).

The second term U_V is a constraint potential that prohibits bond length ℓ_{ij} from being out of the range $\ell_{\min} \leq \ell_{ij} \leq \ell_{\max}$, with $\ell_{\min} = 0.01d$ and $\ell_{\max} = 3d$. The lattice spacing d is fixed to two different values in the simulations to check the influence of surface tension σ [Eq. (16)]. The vertex movements are constrained inside \mathcal{D} by the fixed frame of side lengths L_x and L_y in Fig. 17(a) and by the condition for nonfolding triangles in Fig. 18(c). These constraints can also be written as constraint potentials; however, we omit these potentials for simplicity. Note that $S_1/N = 1$ is satisfied in the case without any constraints on the bond length, such as the constraint on the side lengths L_x and L_y (Fig. 17) and the constraint U_V , due to the scale-invariant property of the partition function

two-dimensional surfaces, as shown in Fig. 19. In the isotropic case, $\chi_0 \rightarrow \infty$ in Eq. (B2), we have $\chi_{ij}^u/\chi_{kl}^u \rightarrow 1$ and $\gamma_{ij} \rightarrow 2/3$ from Eq. (C3), and therefore, $2\gamma_{ij}^u \rightarrow 4/3$. Thus, using a suitable normalization factor in the definition of γ_{ij}^u in Eq. (C3), we can write Δu_i in Eq. (C9) as the standard network Laplacian $\Delta u_i \rightarrow \sum_{ij} (A_{ij} - k_i \delta_{ij})$.

APPENDIX D: DISCRETE HAMILTONIAN FOR THE MONTE CARLO UPDATE OF IDOF $\vec{\tau}$

(Appendix E for further detail). The term $U_{\mathcal{G}}$ for the fluid model is a constraint potential that enforces $4 \leq q_i \leq 9$ for the coordination number q_i , which is the total number of bonds connected to vertex i [Fig. 21(a)].

The term S_u is given by Eq. (C3), and S_v is obtained from S_u by replacing u with v . S_τ represents the interaction energy for the nearest-neighbor pairs of $\vec{\tau}_i$ and $\vec{\tau}_j$. An additional assumption is that an external force \vec{F} aligns $\vec{\tau}$ along the direction of \vec{F} . This interaction is described by the final term S_τ^F .

Here we comment on the implications of the definitions of χ_{ij}^u and χ_{ij}^v in Eq. (B2). Suppose $\vec{\tau}_i$ aligns along the \vec{e}_{ij} axis; then, χ_{ij}^u and, consequently, the interaction coefficient γ_{ij}^u of S_u in Eq. (D2) increase along the \vec{e}_{ij} axis, resulting in a strong correlation between u_i and u_j . Therefore, if all $\vec{\tau}_i$ are aligned along the x axis by $\vec{F} = (F, 0)$, then the interaction between u_i and u_j is strong (weak) on bond ij , which is almost or relatively parallel (perpendicular) to the x axis, and as a consequence, the direction-dependent γ_{ij}^u makes D_u large (small) along the x (y) direction. This is the pattern alignment mechanism for the variable u induced by external \vec{F} . We should emphasize that the definition of χ_{ij}^v is opposite to that

of χ_{ij}^u in Eq. (B2), even though the pattern direction of v is the same as that of u . However, if the expression of χ_{ij}^v is the same as that of χ_{ij}^u , then relatively weak anisotropic patterns also emerge along the same direction parallel to \vec{F} . This situation corresponds to cases $a > 1$ and $b > 1$ with $c_v^u > 1$ in Eqs. (2), (3), and (4). In contrast, under the definitions in Eq. (B2), if $\vec{\tau}_i$ is aligned along the x direction, then the strongest anisotropy appears, implying that χ_{ij}^u and χ_{ij}^v in Eq. (B2) correspond to the conditions $a > 1$ and $b < 1$ shown in Fig. 4(g). Thus, we consider that the definitions of χ_{ij}^u and χ_{ij}^v in Eq. (B2) describe the competing nature of u and v .

APPENDIX E: COMPUTATIONAL DOMAIN SPANNED BY A MEMBRANE WITH A NONTRIVIAL SURFACE TENSION

In this Appendix, we present detailed information on the computational domain \mathcal{D} bounded by a fixed frame [Fig. 22(a)] for PBCs in Figs. 17 and 19(a). As mentioned in Sec. III, this domain \mathcal{D} has an internal structure described by vertex positions $\vec{r}_i \in \mathbf{R}^2$, $1 \leq i \leq N$, and these \vec{r}_i are regarded as membranes [40–42,44–47], which are classical mechanical N -particle systems governed by the spring potential or the Gaussian bond potential $S_1(\vec{r})$ and by several constraints imposed on \vec{r}_i . Mainly due to S_1 and the boundary

frame, membrane \mathcal{D} is exposed to tensile stress σ , which originates from the so-called scale-invariant property of the partition function, as mentioned in Sec. III [48]. This property is common to both the fixed and fluid models; here we use Z_{fix} in Eq. (13) for simplicity.

First, we note that the variables \vec{r}_i are integrated in Z_{fix} , i.e., $\int \prod_i d\vec{r}_i \exp(-S)$, corresponding to $2N$ -dimensional multiple integrations. Here we rewrite S as $S = S_1 + U_{\text{fr}}(A) + S_{\text{other}}$, where $U_{\text{fr}}(A)$ is the potential for fixing the frame area A to $A = L_x L_y$ and not included in S of Eq. (12), and S_{other} is the remaining term in S . Note that $S_1 = \sum_{ij} \ell_{ij}^2$ and $U_{\text{fr}}(A)$ depend on \vec{r} and that S_{other} is independent of \vec{r} . We replace \vec{r} with $\vec{r}_\beta = \beta \vec{r}$ in Z_{fix} with the scale parameter $\beta (\geq 1)$. This replacement constitutes a simple variable change in integration $\int d\vec{r}_i \rightarrow \beta^2 \int d\vec{r}_i$, $S_1 \rightarrow \beta^2 S_1, \dots$, and it does not change Z_{fix} ; therefore, we have $Z_{\text{fix}}(\vec{r}) = Z_{\text{fix}}(\vec{r}_\beta)$, where

$$Z_{\text{fix}}(\vec{r}_\beta) = \beta^{2N} \int \prod_i d\vec{r}_i \exp[-\beta^2 S_1 - U_{\text{fr}}(A_\beta) - S_{\text{other}}]. \quad (\text{E1})$$

In the expression $U_{\text{fr}}(A_\beta)$, A_β is given by $A_\beta = \beta^{-2} A$ because the fixed frame means that the area scales as $A \rightarrow A_\beta = \beta^{-2} A$ according to the scale change $\vec{r} \rightarrow \beta \vec{r}$. By differentiating both sides of $Z_{\text{fix}}(\vec{r}) = Z_{\text{fix}}(\vec{r}_\beta)$ with respect to β and by fixing $\beta \rightarrow 1$, we have

$$\begin{aligned} 0 &= \frac{\partial}{\partial \beta} Z_{\text{fix}}(\vec{r}_\beta) \Big|_{\beta=1} \\ &= \frac{\partial}{\partial \beta} \left\{ \beta^{2N} \int \prod_i d\vec{r}_i \exp[-\beta^2 S_1 - U_{\text{fr}}(A_\beta) - S_{\text{other}}] \right\} \Big|_{\beta=1} \\ &= 2N \beta^{-1} Z_{\text{fix}}(\vec{r}_\beta) \Big|_{\beta=1} + 2\beta^{2N+1} \int \prod_i d\vec{r}_i S_1 \exp[-S(\vec{r}_\beta)] \Big|_{\beta=1} + \frac{\partial Z_{\text{fix}}(\vec{r}_\beta)}{\partial A_\beta} \frac{\partial A_\beta}{\partial \beta} \Big|_{\beta=1} \\ &= 2N Z_{\text{fix}}(\vec{r}) - 2 \int \prod_i d\vec{r}_i S_1 \exp[-S(\vec{r})] - 2A \frac{\partial Z_{\text{fix}}(\vec{r})}{\partial A}, \end{aligned} \quad (\text{E2})$$

where $\frac{\partial A_\beta}{\partial \beta} \Big|_{\beta=1} = \frac{\partial \beta^{-2} A}{\partial \beta} \Big|_{\beta=1} = -2A$ is used in the final term of the third line. We note that the boundary of the surface expanded by $\beta (\geq 1)$ is identified with the fixed frame only when $\beta \rightarrow 1$ [Fig. 22(b)]. Multiplying $2^{-1} Z_{\text{fix}}(\vec{r})^{-1}$ by the final expression in Eq. (E2), we obtain

$$0 = N - \langle S_1 \rangle - \frac{A}{Z_{\text{fix}}(\vec{r})} \frac{\partial Z_{\text{fix}}(\vec{r})}{\partial A}. \quad (\text{E3})$$

Since $\langle S_1 \rangle = \langle \sum_{ij} \ell_{ij}^2 \rangle$ can be replaced by $\sum_{ij} \langle \ell_{ij}^2 \rangle = \sum_{ij} \langle \ell^2 \rangle = \langle \ell^2 \rangle \sum_{ij} 1 = N_B \langle \ell^2 \rangle = 3N \langle \ell^2 \rangle$, we have the mean-squared bond length $\langle \ell^2 \rangle$

$$\langle \ell^2 \rangle = \frac{1}{3} - \frac{1}{3N} \frac{A}{Z_{\text{fix}}(\vec{r})} \frac{\partial Z_{\text{fix}}(\vec{r})}{\partial A}. \quad (\text{E4})$$

If the boundary frame for the PBCs is not assumed, then the second term on the right-hand side is unnecessary. Hence, we

have $\langle \ell^2 \rangle = 1/3 (\Leftrightarrow \langle S_1 \rangle / N = 1)$, as mentioned in the main text.

The problem lies in how to evaluate the second term when a frame is present. The potential $U_{\text{fr}}(A)$ expressed as U_V in Eq. (D2) is not differentiable. Therefore, to evaluate $\frac{\partial Z_{\text{fix}}(\vec{r})}{\partial A}$ for surfaces with a fixed frame, we regard the membrane of the N -particle system bounded by the frame as a sheet of area A without the internal structure associated with the N particles. For this simple surface of area A , its free energy $F(A)$ is given by $F(A) = \sigma A$, where σ is the surface tension. Therefore, the partition function can also be expressed as $Z(A) = \exp[-F(A)]$. Thus, $\partial Z_{\text{fix}}(\vec{r}) / \partial A$ can be evaluated by replacing $Z_{\text{fix}}(\vec{r})$ with $\exp[-F(A)] = \exp(-\sigma A)$, and we have $\langle \ell^2 \rangle = 1/3 + \sigma A / (3N)$ from Eq. (E4); therefore,

$$\begin{aligned} \sigma &= \frac{3N}{A} \left(\langle \ell^2 \rangle - \frac{1}{3} \right) \simeq \frac{3}{d^2} \left(\langle \ell^2 \rangle - \frac{1}{3} \right), \\ A &= L_x L_y = (n_x - 1)(n_y - 1)d^2, \end{aligned} \quad (\text{E5})$$

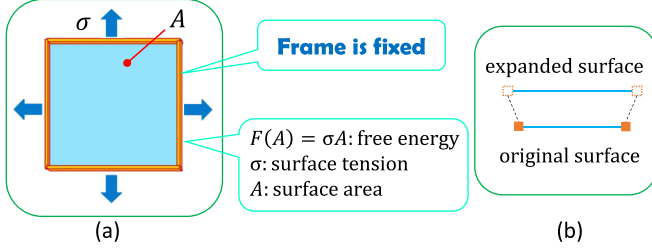


FIG. 22. (a) Surface enclosed by a fixed boundary frame of area A under a constant surface tension σ . This surface has a mechanical free energy $F(A) = \sigma A (= \int^A \sigma dA)$ because σ is constant and isotropic. (b) Illustrations of the original surface with a boundary frame and a surface expanded by a scale parameter $\beta (\geq 1)$.

where $L_x, L_y, n_x,$ and n_y are shown in Fig. 17. Thus, σ depends on the lattice spacing d . In this expression, $\langle \ell^2 \rangle$ is originally $\gamma \langle \ell^2 \rangle$ with the tension coefficient $\gamma (=1)$, and hence, $\langle \ell^2 \rangle - \frac{1}{3}$ has the simulation unit of 1, which is of physical unit $k_B T$. Therefore, the physical unit of the surface tension σ is given by $\text{kg s}^{-2} = \text{Nm}^{-1}$.

APPENDIX F: DIRECTION-DEPENDENT DIFFUSION CONSTANTS AND EFFECTIVE ENERGIES

In this Appendix, we describe the direction-dependent diffusion constants and corresponding effective direction-dependent energies obtained by the discrete Laplace operator in Eq. (11). First, we note that the unit tangential vector \vec{e}_{ij} from vertices i to j can be decomposed into $\vec{e}_{ij} = \vec{e}_{ij}^x + \vec{e}_{ij}^y$ [Fig. 21(b)]. Then, by using the angle θ_{ij} and the relations $1 = \vec{e}_{ij} \cdot \vec{e}_{ij} = (e_{ij}^x)^2 + (e_{ij}^y)^2 = \cos^2 \theta_{ij} + \sin^2 \theta_{ij}$ satisfying $\cos^2 \theta_{ij} = \sin^2 \theta_{ij} = 1/2$ for $\theta_{ij} = \pi/4$, γ_{ij}^u is decomposed into two different parts, which can be considered the x and y components:

$$\gamma_{ij}^u = \gamma_{ij}^{u,x} + \gamma_{ij}^{u,y} = \gamma_{ij}^u \cos^2 \theta_{ij} + \gamma_{ij}^u \sin^2 \theta_{ij}. \quad (\text{F1})$$

This γ_{ij}^u is considered to have values on bond ij . Here we assume an anisotropic case in which γ_{ij}^u is very large on bonds that are almost parallel to the x axis [$\Leftrightarrow \theta_{ij} \simeq 0$ in Fig. 21(b)]. In this case, $\gamma_{ij}^{u,x} > \gamma_{ij}^{u,y}$ on bonds ij almost parallel to the x axis because $\cos^2 \theta_{ij} \simeq 1$ and $\sin^2 \theta_{ij} \simeq 0$. Thus, we have the direction-dependent diffusion constants defined by

$$D_u^x = \frac{1}{\sum_{ij} 1} \sum_{ij} \gamma_{ij}^{u,x} = \frac{1}{N_B} \sum_{ij} \gamma_{ij}^u \cos^2 \theta_{ij},$$

$$D_u^y = \frac{1}{\sum_{ij} 1} \sum_{ij} \gamma_{ij}^{u,y} = \frac{1}{N_B} \sum_{ij} \gamma_{ij}^u \sin^2 \theta_{ij}, \quad (\text{F2})$$

where $N_B = \sum_{ij} 1 (=3N)$ denotes the total number of bonds.

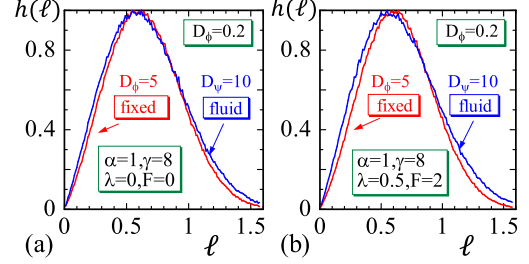


FIG. 23. Bond length distribution $h(\ell)$ vs ℓ of the fixed model (red) and fluid model (blue) with (a) $\lambda = 0, \vec{F} = (0, 0)$ and (b) $\lambda = 0.5, \vec{F} = (0, 2)$, which correspond to the isotropic and anisotropic patterns plotted in Figs. 6(a) and 7(a) and in Figs. 6(d) and 7(d), respectively. The cutoff is $\ell_{\max} = 3d = 1.575$, with a lattice spacing of $d (=0.525)$. The curves $h(\ell)$ vs ℓ for $d = 0.41$ are almost the same as those in the figures.

Direction-dependent energies S_u^x and S_u^y in Eq. (18) corresponding to D_u^x and D_u^y can also be obtained using S_u in Eq. (C3):

$$S_u = \sum_{ij} \gamma_{ij}^u (u_i - u_j)^2 = \sum_{ij} (\gamma_{ij}^u \cos^2 \theta_{ij} + \gamma_{ij}^u \sin^2 \theta_{ij})$$

$$\times (u_i - u_j)^2$$

$$= \frac{1}{N_B} \sum_{ij} \gamma_{ij}^u \cos^2 \theta_{ij} \frac{\sum_{ij} \gamma_{ij}^u \cos^2 \theta_{ij} (u_i - u_j)^2}{(1/N_B) \sum_{ij} \gamma_{ij}^u \cos^2 \theta_{ij}}$$

$$+ \frac{1}{N_B} \sum_{ij} \gamma_{ij}^u \sin^2 \theta_{ij} \frac{\sum_{ij} \gamma_{ij}^u \sin^2 \theta_{ij} (u_i - u_j)^2}{(1/N_B) \sum_{ij} \gamma_{ij}^u \sin^2 \theta_{ij}}$$

$$= D_u^x S_u^x + D_u^y S_u^y. \quad (\text{F3})$$

APPENDIX G: BOND LENGTH DISTRIBUTION

In this Appendix, we plot the bond length distribution $h(\ell)$ on fixed and fluid lattices of size $N = 6400$ in Figs. 23(a) and 23(b). The lattice size is the same as that assumed for the calculations of the diffusion constants D_u^x, D_u^y and σ , as plotted in Figs. 8–10, respectively. The total numbers of iterations n_{itr} and n_{MC} are also the same as those in Eq. (19). The coefficients are $(D_u, D_v) = (0.2, 5)$ in the fixed model, and $(D_u, D_v) = (0.2, 10)$ in the fluid model. These parameters, including (α, γ) , are the same as those assumed in the calculation of isotropic and anisotropic snapshots in Figs. 6(a) and 6(d) for the fixed model and in Figs. 7(a) and 7(d) for the fluid model. From both the isotropic and anisotropic cases in Fig. 7(a) and 7(b), we find that the distribution of $h(\ell)$ on the fluid lattice is slightly wide in both directions of small and large ℓ . This slightly broad spectrum of $h(\ell)$ in the fluid model is due to the free diffusion of the vertices.

- [1] A. M. Turing, The chemical basis of morphogenesis, *Philos. Trans. R. Soc. Lond.* **237**, 37 (1952).
 [2] A. Gierer and H. Meinhardt, A theory of biological pattern formation, *Kybernetik* **12**, 30 (1972).

- [3] A. Koch and H. Meinhardt, *Rev. Mod. Phys.* **66**, 1481 (1994).
 [4] D. Fitzhugh, Impulses and physiological states in theoretical models of nerve membrane, *Biophys. J.* **1**, 446 (1961).

- [5] J. Nagumo, S. Arimoto, and S. Yoshizawa, An active pulse transmission line simulating nerve Axon, *Proc. IRE.* **2061** (1962).
- [6] T. Sekimura, A. Madzvamuse, A. J. Wathen, and P. K. Maini, A model for colour pattern formation in the butterfly wing of *Papilio dardanus*, *Proc. R. Soc. Lond. B* **267**, 851 (2000).
- [7] S. Kondo and T. Miura, Reaction-diffusion model as a framework for understanding biological pattern formation, *Science* **329**, 1616 (2010).
- [8] D. Bullara and Y. De Decker, Pigment cell movement is not required for generation of Turing patterns in zebrafish skin, *Nat. Commun.* **6**, 6971 (2015).
- [9] Z. Tan, S. Chen, X. Peng, L. Zhang, and C. Gao, Polyamide membranes with nanoscale Turing structures for water purification, *Science* **360**, 518 (2018).
- [10] Y. Fuseya, H. Katsuno, K. Behnia, and A. Kapitulnik, Nanoscale Turing patterns in a bismuth monolayer, *Nat. Phys.* **17**, 1031 (2021).
- [11] H. Nakao and A. S. Mikhailov, Turing patterns in network-organized activator-inhibitor systems, *Nat. Phys.* **6**, 544 (2010).
- [12] T. Carletti and H. Nakao, Turing patterns in a network-reduced FitzHugh-Nagumo model, *Phys. Rev. E* **101**, 022203 (2020).
- [13] M. Asllani, J. D. Challenger, F. S. Pavone, L. Sacconi and D. Fanelli, The theory of pattern formation on directed networks, *Nat. Commun.* **5**, 4517 (2014).
- [14] M. Asllani, D. M. Busiello, T. Carletti, D. Fanelli, and G. Planchon, Turing patterns in multiplex networks, *Phys. Rev. E* **90**, 042814 (2014).
- [15] J. Petit, M. Asllani, D. Fanelli, B. Lauwens, and T. Carletti, Pattern formation in a two-component reaction-diffusion system with delayed processes on a network, *Physica A* **462**, 230 (2016).
- [16] A. Alexandre, M. Lavaud, N. Fares, E. Millan, Y. Louyer, T. Salez, Y. Amarouchene, T. Guérin, and D. S. Dean, Non-gaussian diffusion near surfaces, *Phys. Rev. Lett.* **130**, 077101 (2023).
- [17] P. C. Bressloff and J. M. Newby, Stochastic models of intracellular transport, *Rev. Mod. Phys.* **85**, 135 (2013).
- [18] F. Höfling and T. Franosch, Anomalous transport in the crowded world of biological cells, *Rep. Prog. Phys.* **76**, 046602 (2013).
- [19] I. M. Sokolov, J. Klafter, and A. Blumen, Fractional kinetics, *Phys. Today* **55(11)**, 48 (2002).
- [20] R. Metzler and J. Klafter, The restaurant at the end of the random walk: Recent developments in the description of anomalous transport by fractional dynamics, *J. Phys. A: Math. Gen.* **37**, R161 (2004).
- [21] G. Ariel, A. Shklarsh, O. Kalisman, C. Ingham, and E. Ben-Jacob, From organized internal traffic to collective navigation of bacterial swarms, *New J. Phys.* **15**, 125019 (2013).
- [22] G. Ariel, A. Rabani, S. Benisty, J. D. Partridge, R. M. Harshey, and A. Be'er, Swarming bacteria migrate by Lévy Walks, *Nat. Commun.* **6**, 8396 (2015).
- [23] S. Kondo and R. Asai, A reaction-diffusion wave on the skin of the marine angelfish *Pomacanthus*, *Nature (Lond.)* **376**, 765 (1995).
- [24] H. Shoji, A. Mochizuki, Y. Iwasa, M. Hirata, T. Watanabe, S. Hioki, and S. Kondo, Origin of Directionality in the Fish Stripe Pattern, *Dev. Dynam.* **226**, 627 (2003).
- [25] R. Iwamoto and H. Shoji, Kakusan Ihousei Turing pattern, *RIMS Kokyuroku* **2087**, 108 (2018).
- [26] C. Varea, J. L. Aragón, and R. A. Barrio, Turing patterns on a sphere, *Phys. Rev. E* **60**, 4588 (1999).
- [27] A. L. Krause, M. A. Ellis, and R. A. Van Gorder, Influence of curvature, growth, and anisotropy on the evolution of Turing patterns on growing manifolds, *Bull. Math. Biol.* **81**, 759 (2019).
- [28] A. L. Krause, E. A. Gaffney, P. K. Maini, and V. Klica, Modern perspectives on near-equilibrium analysis of Turing systems, *Philos. Trans. R. Soc. A* **379**, 20200268 (2021).
- [29] H. Koibuchi, M. Okumura, and S. Noro, Finsler geometry modeling for anisotropic diffusion in Turing patterns, *J. Phys.: Conf. Ser.* **1730**, 012035 (2021).
- [30] H. Koibuchi, F. Kato, G. Diguët, and T. Uchimoto, Origin of anisotropic diffusion in Turing patterns, [arXiv:2208.09977](https://arxiv.org/abs/2208.09977).
- [31] H. Koibuchi and H. Sekino, Monte Carlo studies of a Finsler geometric surface model, *Physica A* **393**, 37 (2014).
- [32] Y. Takano and H. Koibuchi, J-shaped stress-strain diagram of collagen fibers: Frame tension of triangulated surfaces with fixed boundaries, *Phys. Rev. E* **95**, 042411 (2017).
- [33] E. Proutorov, N. Matsuyama and H. Koibuchi, Finsler geometry modeling and Monte Carlo study of liquid crystal elastomers under electric fields, *J. Phys.: Condens. Matter* **30**, 405101 (2018).
- [34] S. El Hog, F. Kato, H. Koibuchi, and H. T. Diep, Finsler geometry modeling and Monte Carlo study of skyrmion shape deformation by uniaxial stress, *Phys. Rev. B* **104**, 024402 (2021).
- [35] S. El Hog, F. Kato, S. Hongo, H. Koibuchi, G. Diguët, T. Uchimoto, and H. T. Diep, The stability of 3D skyrmions under mechanical stress studied via Monte Carlo calculations, *Results Phys.* **38**, 105578 (2022).
- [36] K. John, S. Alonso, and M. Bär, Traveling waves and global oscillations triggered by attractive molecular interactions in an excitable system, *Phys. Rev. E* **90**, 052913 (2014).
- [37] R. Friedberg and H.-C. Ren, Field theory on a computationally constructed random lattice, *Nucl. Phys. B* **235**, 310 (1984).
- [38] N. Metropolis, A. W. Rosenbluth, M. N. Rosenbluth, and A. H. Teller, Equation of state calculations by fast computing machines, *J. Chem. Phys.* **21**, 1087 (1953).
- [39] D. P. Landau, Finite-size behavior of the simple-cubic Ising lattice, *Phys. Rev. B* **13**, 2997 (1976).
- [40] Y. Kantor and D. R. Nelson, Phase transitions in flexible polymeric surfaces, *Phys. Rev. A* **36**, 4020 (1987).
- [41] G. Gompper and D. M. Kroll, Shape of inflated vesicles, *Phys. Rev. A* **46**, 7466 (1992).
- [42] H. Koibuchi and T. Kuwahata, First-order phase transition in the tethered surface model on a sphere, *Phys. Rev. E* **72**, 026124 (2005).
- [43] M. Doi and F. Edwards, *The Theory of Polymer Dynamics* (Oxford University Press, Oxford, 1986).

- [44] J.-S. Ho and A. Baumgärtner, Simulations of fluid self-avoiding membranes, [Europhys. Lett.](#) **12**, 295 (1990).
- [45] L. Peliti and S. Leibler, Effects of thermal fluctuations on systems with small surface tension, [Phys. Rev. Lett.](#) **54**, 1690 (1985).
- [46] W. Z. Helfrich, Elastic properties of lipid bilayers: Theory and possible experiment, [Naturforsch](#) **28c**, 693 (1973).
- [47] D. Nelson, *The Statistical Mechanics of Membranes and Interfaces*, in *Statistical Mechanics of Membranes and Surfaces, Second Edition*, edited by D. Nelson, T. Piran, and S. Weinberg (World Scientific, Singapore, 2004), p. 1.
- [48] J. F. Wheeler, Random surfaces: From polymer membranes to strings, [J. Phys. A: Math. Gen.](#) **27**, 3323 (1994).